Cellular/Molecular

Drosophila Homolog of the Human Carpenter Syndrome Linked Gene, *MEGF8*, Is Required for Synapse Development and Function

Shuting Chen,[1,2] Anand Venkatesan,[1] Yong Qi Lin,[3] Jing Xie,[1,2] Gregory Neely,[3] Swati Banerjee,[1] and Manzoor A. Bhat[1]

[1]Department of Cellular and Integrative Physiology, Joe R. and Teresa Lozano Long School of Medicine, University of Texas Health Science Center San Antonio, San Antonio, Texas 78229, [2]Second Xiangya Hospital of Central South University, Changsha, Hunan 410011, China, and [3]Dr. John and Anne Chong Lab for Functional Genomics, Charles Perkins Centre and School of Life and Environmental Sciences, University of Sydney, Sydney, New South Wales Australia 2006

Drosophila **multiple epidermal growth factor-like domains 8 (dMegf8) is a homolog of human *MEGF8*. *MEGF8* encodes a multidomain transmembrane protein which is highly conserved across species. In humans, *MEGF8* mutations cause a rare genetic disorder called Carpenter syndrome, which is frequently associated with abnormal left-right patterning, cardiac defects, and learning disabilities. *MEGF8* is also associated with psychiatric disorders. Despite its clinical relevance, *MEGF8* remains poorly characterized; and although it is highly conserved, studies on animal models of Megf8 are also very limited. The presence of intellectual disabilities in Carpenter syndrome patients and association of *MEGF8* with psychiatric disorders indicate that mutations in *MEGF8* cause underlying defects in synaptic structure and functions. In this study, we investigated the role of *Drosophila* dMegf8 in glutamatergic synapses of the larval neuromuscular junctions (NMJ) in both males and females. We show that dMegf8 localizes to NMJ synapses and is required for proper synaptic growth. *dMegf8* mutant larvae and adults show severe motor coordination deficits. At the NMJ, *dMegf8* mutants show altered localization of presynaptic and postsynaptic proteins, defects in synaptic ultrastructure, and neurotransmission. Interestingly, *dMegf8* mutants have reduced levels of the Type II BMP receptor Wishful thinking (*Wit*). *dMegf8* displays genetic interactions with *neurexin-1* (*dnrx*) and *wit*, and in association with Dnrx and Wit plays an essential role in synapse organization. Our studies provide insights into human MEGF8 functions and potentially into mechanisms that may underlie intellectual disabilities observed in Carpenter syndrome as well as MEGF8-related synaptic structural and/or functional deficits in psychiatric disorders.**

Key words: **BMP signaling; Carpenter syndrome; *Drosophila* larval NMJ; MEGF8; Neurexin-1; synapses**

Significance Statement

Carpenter syndrome, known for over a century now, is a genetic disorder linked to mutations in *Multiple Epidermal Growth Factor-like Domains 8* (*MEGF8*) gene and associated with intellectual disabilities among other symptoms. *MEGF8* is also associated with psychiatric disorders. Despite the high genetic conservation and clinical relevance, the functions of *MEGF8* remain largely uncharacterized. Patients with intellectual disabilities and psychiatric diseases often have an underlying defect in synaptic structure and function. This work defines the role of the fly homolog of human *MEGF8*, *dMegf8*, in glutamatergic synapse growth, organization, and function and provide insights into potential functions of *MEGF8* in human central synapses and synaptic mechanisms that may underlie psychiatric disorders and intellectual disabilities seen in Carpenter syndrome.

Received Mar. 6, 2022; revised July 29, 2022; accepted Aug. 3, 2022.

Author contributions: S.C., S.B., and M.A.B. designed research; S.C., A.V., Y.Q.L., J.X., and S.B. performed research; S.C., A.V., J.X., G.N., S.B., and M.A.B. analyzed data; S.C., S.B., and M.A.B. wrote the first draft of the paper; S.C., A.V., Y.Q.L., J.X., G.N., S.B., and M.A.B. edited the paper.

This work was supported by the Zachry Foundation for Neuroscience Research and the University of Texas Health Science Center at San Antonio to M.A.B. We thank all members of the S.B. and M.A.B. laboratories for helpful discussions; and the Electron Microscopy Core Facility at UT Health for assistance.

The authors declare no competing financial interests.

Correspondence should be addressed to Swati Banerjee at banerjees@uthscsa.edu or Manzoor A. Bhat at bhatm@uthscsa.edu.

https://doi.org/10.1523/JNEUROSCI.0442-22.2022

Introduction

Carpenter syndrome (CS), a rare genetic disorder with multiple congenital anomalies, was first described by George Carpenter (Carpenter, 1901). CS patients often present a variety of developmental defects at a very young age, including craniosynostosis, musculoskeletal abnormalities (mostly in fingers and toes), congenital heart disease, and intellectual disabilities (Taravath and Tonsgard, 1993; Hidestrand et al., 2009). Other clinical features, such as hypogenitalism, umbilical hernia, and obesity, have also

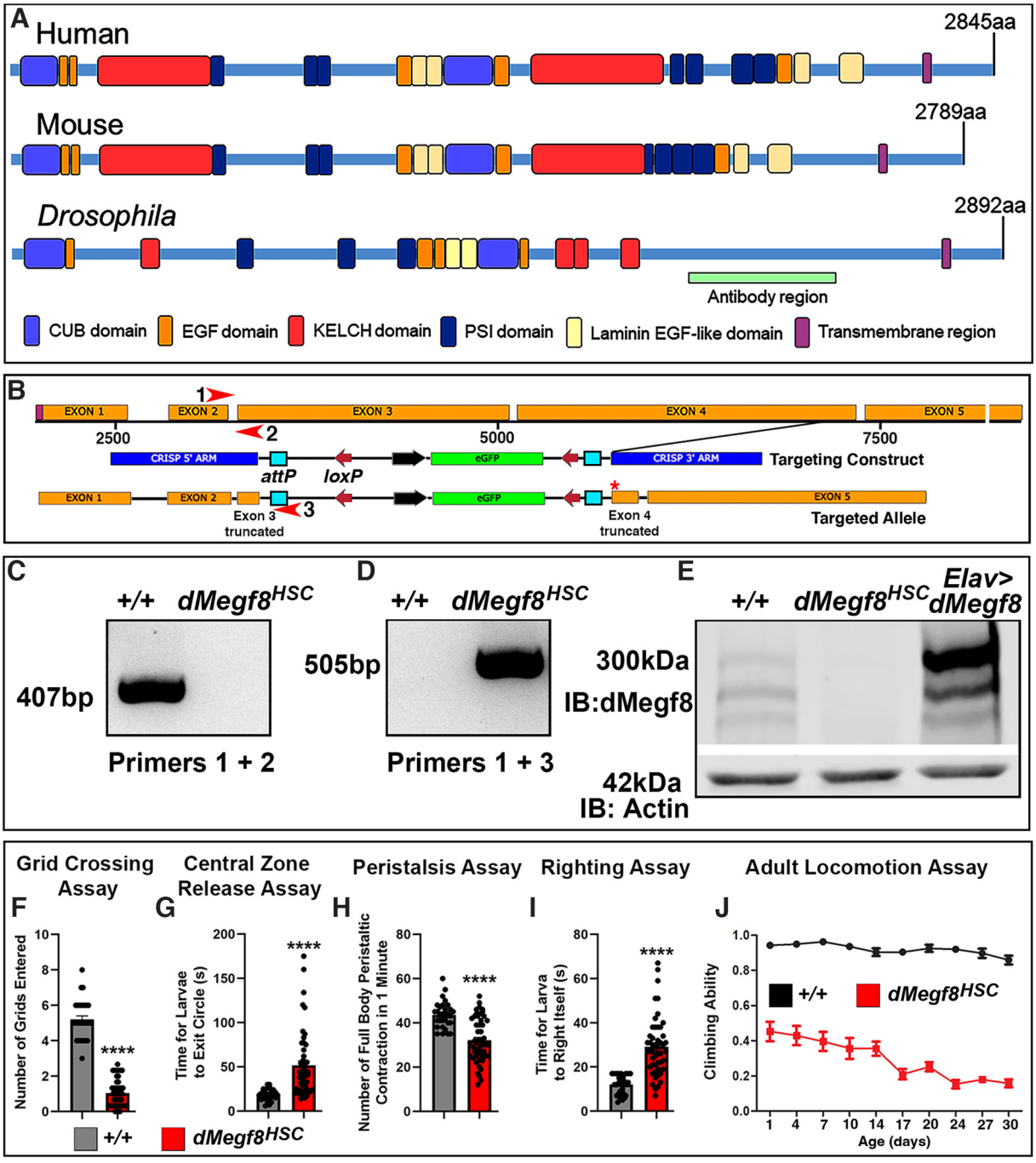

Figure 1. Generation of *dMegf8* mutants. ***A***, Protein domain structure of human MEGF8, mouse Megf8, and *Drosophila* dMegf8. Green bar represents the antibody region in dMegf8. ***B***, Genomic structure of *dMegf8* showing exons 1-5. The targeting construct using CRISPR/Cas9 for recombination and the final targeted allele of $dMegf8^{HSC}$ is shown. Blue boxes next to *loxP* sites on both sides represent phage C31 integration sites referred to as *attP* sites in the targeting vector. Red arrows with numbers indicate location of the primers for genotyping that differentiate the WT and the $dMegf8^{HSC}$ mutants. ***C***, ***D***, PCR confirmation of the targeted deletion using primer combinations 1 + 2 for WT and 1 + 3 for $dMegf8^{HSC}$ mutants in ***B***. ***E***, Immunoblot analysis of dMegf8 showing presence of dMegf8 in WT, loss of dMeg8 in $dMegf8^{HSC}$ mutants, and overexpression of dMegf8 in *elav>dMegf8*. The blot was probed for actin as loading control. ***F–I***, WT (+/+) and $dMegf8^{HSC}$ larval locomotor behaviors assayed by measuring the number of 0.5 cm^2 grids crossed in 30 s (***F***), time taken in seconds for larvae to exit a circle of 1.5 cm in diameter (***G***), number of full body peristaltic contractions in 1 min (***H***), and time taken in seconds for larvae to right themselves when turned on their dorsal surface (***I***). $n = 50$ larvae. Data are mean ± SEM. $t_{(46.49)} = 18.22$, $^{****}p < 0.0001$ (Welch's Student's *t* test) (***F***), $t_{(78)} = 4.833$, $^{****}p < 0.0001$ (unpaired Student's *t* test) (***G***), $t_{(78)} = 5.753$, $^{****}p < 0.0001$ (unpaired Student's *t* test) (***H***), and $t_{(78)} = 6.863$, $^{****}p < 0.0001$ (unpaired Student's *t* test) (***I***). ***J***, Adult locomotion assay using climbing ability of WT (+/+) (black) and $dMegf8^{HSC}$ mutants (red) flies. $n = 50$ flies. Data are mean ± SEM. Interaction: $F_{(9,80)} = 4.579$, $^{****}p < 0.0001$ (two-way ANOVA test).

been reported (Alessandri et al., 2010; Haye et al., 2014). Genome-wide sequence analyses identified three single nucleotide polymorphisms in the *Multiple Epidermal Growth Factor-like Domains 8* (*MEGF8*) gene that showed association with the CS (Twigg et al., 2012). *MEGF8* has also been implicated in neuropsychiatric disorders, such as schizophrenia (Bersani et al., 2003; Cox and Butler, 2015; Giacopuzzi et al., 2017).

Human *MEGF8* is clinically relevant, and its homologs are highly conserved across species and encode a multidomain transmembrane protein (Fig. 1). Murine *Megf8* is involved in bone

morphogenetic protein (BMP) signaling and mutations in mice *Megf8* disrupt axon guidance and lead to defects that phenotypically resemble human CS, including deformities of the limb, heart, and abnormal left-right patterning (Engelhard et al., 2013). *Megf8*, together with *Mgrn1*, catalyzes the ubiquitination and degradation of the Hedgehog pathway signaling molecules that coordinate cell–cell communication required for spinal cord and heart development (Jenkins et al., 2007; Pusapati et al., 2018; Kong et al., 2020). These findings suggest that *Megf8* functions in multiple intracellular signaling pathways and may modulate different cellular processes during development. Despite these observations on the role of Megf8 in different developmental events and in neuronal function, it has remained unclear whether Megf8 has any role in synaptic development and function. Most importantly, intellectual disabilities seen in CS patients as well as the association of human MEGF8 with psychiatric disorders, such as schizophrenia, point toward a potential role of MEGF8 in synaptic processes as many of the learning disabilities and psychiatric disorders have underlying defects in synaptic development and/or function (Valnegri et al., 2012; Giacopuzzi et al., 2017; Obi-Nagata et al., 2019).

The *Drosophila* neuromuscular junctions (NMJs) have served as an ideal model for studying synapse development and functions (Wu et al., 2010), and have similarities with the mammalian central synapses. Since dMegf8 shows high amino acid sequence and domain homology with vertebrate *Megf8* (Lloyd et al., 2018), studies on dMegf8 will be informative about the role of vertebrate Megf8 proteins. While not much is known about *dMegf8*, several genome-wide RNAi-screens found that *dMegf8* knockdown resulted in cell death or reduced cell viability phenotype (Chittaranjan et al., 2009; Mummery-Widmer et al., 2009). In a machine-learning study, *dMegf8* was found to be one of the putative synaptic genes indicating a potential involvement of dMegf8 in synapse assembly and function (Pazos Obregon et al., 2015). A recent report showed that *dMegf8* mutants have disrupted larval denticle belts and bristle formation, and a delayed transition to third instar larvae associated with larval lethality (Lloyd et al., 2018). There are no published reports on any role of Megf8 in synapse organization or function in any species.

Here we report the generation of *dMegf8* null mutants and show that dMegf8 is expressed both presynaptic and postsynaptically. dMegf8 is required for synaptic growth, and loss of dMegf8 leads to synaptic ultrastructural defects and reduced synaptic transmission. Additionally, genetic rescue experiments support that *dMegf8* is necessary presynaptically for proper NMJ growth. However, synaptic ultrastructural defects resulting from dMegf8 loss are significantly rescued by dMegf8 presynaptic and/or postsynaptic expression. Importantly, *dMegf8* shows genetic interactions with *Drosophila neurexin* (*dnrx*) and the BMP receptor *wishful thinking* (*wit*), and these proteins exist in a biochemical complex to coordinate proper NMJ development. Together, our studies establish the role of dMegf8 in NMJ synaptic development and function, and provide key insights into potential *Megf8* functions in vertebrate synaptic mechanisms that underlie intellectual disabilities seen in CS patients.

Materials and Methods

Fly stocks. The *Drosophila* lines used in this study include *w1118* Canton-S line (used as WT control; kind gift from Vivian Budnik), $dMegf8^{\Delta 8}$ (Lloyd et al., 2018), $dnrx^{273}$, *UAS-dnrx* (Li et al., 2007), and *UAS-wit-GFP* (a gift from Michael O'Connor). To generate *UAS-dMegf8* flies, we obtained a partial *dMegf8* cDNA clone from DGRC (clone *#LD09511*) that encodes a polypeptide containing only the C-terminal amino acids 2089-2892 of the full-length dMegf8RB protein. The remaining 2088 N-terminal amino acids were obtained by RT-PCR using Poly A^+ mRNA isolated from adult fly brains. A full-length clone was assembled containing 10,201 nucleotides representing the largest dMegf8 isoform (*dMegf8 RB*), which was confirmed by sequencing and cloned into *pUAS-attB* vector to create transgenic flies. All other fly stocks, including *Df(2L)7147*, wit^{A12}, and wit^{B11}, and all *Gal4* lines were obtained from the Bloomington Drosophila Stock Center. All flies were maintained at 25°C, 50% humidity and with a 12 h light/dark cycle.

Generation of dMegf8 mutants. To generate a targeted deletion in the *dMegf8* locus that would produce a *dMegf8* null allele, we used CRISPR/Cas9 methodology and procedures established at the GenetiVision company based on the previously reported strategies (Zhang et al., 2014). The targeting construct contained 5′ and 3′ homology arms flanking a GFP expression cassette that replaced the deleted sequences in the *dMegf8* locus. The targeting construct was injected into embryos, and the transgenic flies were tested by PCR analysis using a combination of primers that distinguished the WT and *dMegf8* null alleles (primer 1-5′-GCA CGCTTCAGGTAAGTCGTA-3′, primer 2-5′-GCGGCTTGTGATCCG TAACCT-3′ and primer 3-5′-GATGGGACAAGTCGCCATGT T-3'). Further characterization of the *dMegf8* alleles used standard methodologies.

Larval locomotion assays. The larval locomotion assay was performed as described previously (Banerjee and Riordan, 2018). Briefly, larvae were first washed in distilled water to remove any traces of food before performing various assays. Each larva was acclimatized to the test plate for 1 min before testing. Five trials per larvae were conducted, and the total number of larvae analyzed per genotype was 50.

For the grid crossing assay, individual larvae were placed in the center of a 145-mm-diameter Petri dish, with 2% non-nutritious agar previously poured and allowed to harden covering a graph paper at the bottom with 0.5 cm^2 marked grids. The number of grid line crossings within a 30 s time window was recorded 5 times per larva.

For the central zone release assay, a circular white card 1.5 cm inch diameter was taped to the bottom of the dish to mark the central release zone. Five animals were placed at the center of the release zone. The time taken for each animal to exit the release zone was recorded.

For the peristalsis contraction assay, full body peristalsis contractions (full posterior to anterior movement = 1 contraction) were counted for each larva in 1 min while observing under a dissection microscope.

For the righting assay, larvae were turned on their dorsal surfaces with a fine brush and the time taken to return to their ventral crawling position was recorded.

Adult locomotion assay. To determine the locomotor ability of the flies, adult climbing assay was performed as described previously (Gargano et al., 2005; Xie et al., 2021). Briefly, 10 freshly eclosed male flies were collected in individual vials, and a total of 50 flies for each genotype were analyzed. The assay was started 24 h after CO_2 anesthesia. Flies were gently taped down to the bottom of an empty clear vial, and the number of flies crossing a 10 cm mark drawn from the base of the vial within 10 s were recorded. Each assay was repeated 6 times with a recovery time of 1 min in between, and the mean was calculated. The climbing ability is shown as the percentage of mean number of flies crossing the mark.

Production of dMegf8 *antibodies.* To generate antibodies against the dMegf8 protein, a partial cDNA clone of *dMegf8* that contained two-thirds of the coding sequences of dMegf8 from the 3′-end was obtained from the *DGRC Center* and further confirmed by DNA sequencing. A portion of the *dMegf8* was subcloned (cDNA nucleotide numbers 6706-7323) into *pET28 a(+)* vector and expressed in *Escherichia coli BL21DE3* followed by His-column affinity purification. The recombinant polypeptide was used as an antigen to generate rabbit and guinea pig polyclonal antibodies, which were further tested by immunostaining and immunoblotting methods.

Immunohistochemistry. Wandering third-instar larvae from various genotypes were dissected and fixed in either Bouin's fixative or 4% PFA for 15 min and processed as previously described (Chen et al., 2012; Banerjee et al., 2017). Dnrx signal at NMJ was enhanced using previously described protocols (Li et al., 2007). Primary antibodies used were rabbit

anti-dMegf8 (1:500, this study), FITC-conjugated anti-Hrp (1:250, Jackson ImmunoResearch Laboratories), mouse anti-GluRIIA (1:250) (Marrus et al., 2004; Chen et al., 2012), guinea pig anti-Dnrx (1:250) (Li et al., 2007), rabbit anti-PS1 (p-Mad) (1:500; a gift from P. ten Dijke), and rabbit anti-Smad (1:200, ab52903, Abcam). Anti-PS1 recognizes pMad at the NMJ and anti-Smad antibody, which is a recombinant anti-Smad3 [phospho S423 + S425], recognizes pMad in the ventral nerve cord (VNC) as well as detects pMad on immunoblots (Banerjee et al., 2017; Banerjee and Riordan, 2018). Mouse monoclonal anti-Dlg (1:500, 4F3), anti-BRP (1:250; NC82), and anti-Wit (1:25, 23C7) were obtained from Developmental Studies Hybridoma Bank (DSHB), University of Iowa. Secondary antibodies conjugated to Alexa-488, -568, and -647 (Invitrogen) were used at 1:400 dilution. Confocal images of all dissected larval tissues belonging to the same experimental group were imaged under identical settings with a Carl Zeiss LSM710 confocal microscope, and all image processing was done using Adobe Photoshop software.

Immunoblotting and immunoprecipitations (IPs). The immunoblotting and IP experiments were performed as previously described (Banerjee et al., 2017). Briefly, for immunoblotting of dMegf8, fly heads of desired genotypes were homogenized using a glass homogenizer in a weight/volume ratio of 1:3 in ice-cold lysis buffer containing 50 mM HEPES, pH 7.5, 100 mM NaCl, 1 mM $MgCl_2$, 1 mM $CaCl_2$, 1% NP-40, and 0.5% deoxycholate with protease inhibitors. The lysates were kept on ice for 10 min and centrifuged at 20,000 × *g* for 15 min at 4°C. The resultant supernatant was centrifuged at 100,000 × g for 30 min at 4°C. The membrane pellet was further solubilized in 1 × PBS and used subsequently for IP and immunoblot analyses. For the immunoblotting of third instar larval musculature or VNC and brain lobes without any attached imaginal discs, tissues were homogenized in ice-cold RIPA buffer. The supernatants with equal amounts of proteins from each genotype were separated on SDS-PAGE followed by immunoblotting with appropriate antibodies. For IP studies, fly heads of the appropriate genotypes were processed according to previously described protocols (Banerjee et al., 2017). Each experiment was performed independently 3 times, and the most representative blots are presented. Primary antibodies used for immunoblotting were anti-dMegf8 (1:1000), anti-Dnrx (1:250) (Li et al., 2007), anti-Wit (1:1000, DSHB), anti-Smad (1:150, Abcam), anti-Trio (1:250, DSHB), and anti-β actin (1:10,000, 4967S, Cell Signaling).

Electron microscopy and morphometric analysis. Ultrastructural analyses of third-instar larval NMJs were processed for TEM as previously described (Banerjee et al., 2017). Briefly, third-instar larval fillets were dissected in ice-cold, Jan's 0.1 mM Ca^{2+} saline, pH 7.o2, and subsequently fixed in 4% PFA/1% glutaraldehyde/0.1 M cacodylic acid, pH 7.2, for 30 min at room temperature followed by overnight fixation at 4°C. The fixed fillets were rinsed 3× in 0.1 M cacodylic acid, pH 7.2, and post-fixed in 2% aqueous osmium tetroxide for 1 h, followed by rinsing and dehydration in increasing ethanol concentrations. Samples were incubated for 1 h in propylene oxide and gradually infiltrated in increasing resin to propylene oxide ratio (1:2, overnight; 2:1, at least 6 h; and full resin for 36 h with constant agitation). Samples were embedded in flat silicone molds with Polybed resin and cured in the oven at 55°C for at least 36 h. Five larvae were processed for EM analysis from each of the genotypes. The number of boutons (*n*) analyzed for each genotype is indicated in respective figure legends. ImageJ was used for morphometric analysis of EM images of only Type Ib boutons from A2 and A3 as previously described (Chen et al., 2012; Banerjee et al., 2017).

Electrophysiology. Electrophysiological analysis of larval NMJ was performed as previously described (Shi et al., 2019). All third instar larvae were grown in an incubator at 25°C (65% humidity). All electrophysiological experiments were performed at room temperature, and all recordings were made only from abdominal segment A3, muscle 6 of third-instar larvae, in HL-3 solution (0.5 mM Ca^{2+} and 20 mM $MgCl_2$) (Stewart et al., 1994). Electrophysiological signals were amplified with an Axoclamp 900A, under the control of Clampex 10 (Molecular Devices). Data were collected only when resting potential was <–63 mV. Excitatory junction potentials (EJPs) were evoked by applying currents of 6 ± 3 mA with fixed stimulus duration at 0.3 ms with 0.2 Hz of stimuli rate. Twenty evoked EJPs were recorded for each muscle for analysis. Miniature EJP (mEJP) events were collected for 2 min. The evoked EJP amplitude was corrected by using nonlinear summation (Feeney et al., 1998). The quantal content was calculated from individual muscles by ratio of the averaged EJP and averaged mEJP amplitudes. Statistical analyses of EJP and mEJPs between genotypes were done using Student's *t* test (SigmaPlot 10.0, Systat Software). Error bars indicate mean ± SEM.

Quantification. Bouton number quantifications (*n* = number of larvae analyzed) were performed from muscles 6/7 of abdominal segment 3 (A3) by staining of the body wall musculature preparations with anti-Hrp and anti-Dlg. Fluorescence intensity measurements for dMegf8, Dnrx, Wit, and pMad were quantified from confocal slices of *Z* stack images compressed using maximum projection functions, which were stained in combination with either NC82 or anti-Hrp antibodies. Same ROIs were selected for each channel and used for assessment and quantification of fluorescence intensity using ImageJ. At least 30 NMJ branches from 8 larvae were analyzed for various genotypes. All genotypes listed under the same quantification groups were stained and processed for imaging and quantified under identical parameters and settings. ImageJ (National Institutes of Health) was used for quantification of band intensities of immunoblots from three independent experiments. The intensity of the bands of interest was divided by their respective actin protein blots to control for any possible unequal loading.

Experimental design and statistical analysis. All experiments described above, including microscopy, image processing, and quantification, were performed by trained researchers. All experiments used both sexes, except for adult locomotion assay, in which only male flies were used to exclude the influence of female's oviposition. Larvae and adult flies from the control and experimental groups were reared in the same media and maintained at the same temperature (25°C) and humidity (50%) and were processed identically.

All statistical analyses were performed using the GraphPad Prism software, and data are presented as mean ± SEM. Statistical significance was determined by one way ANOVA followed by *post hoc* Tukey's multiple comparison test and Student's *t* test. Specifically, the adult locomotion assay used two-way ANOVA as there were two independent variables (age and climbing index, Fig. 1*J*). Error bars indicate mean ± SEM. Wherever possible, exact *p* values are provided in the figure legends. For Figure 1*F*, we analyzed the data using Welch's Student's *t* test, assuming unequal variances and unequal sample sizes. For Figure 4*G*, instead of using normal one-way ANOVA, we used Brown-Forsythe and Welch ANOVA, which takes care of unequal sample size issues. Additional information about each statistical test, including degrees of freedom and other statistic-specific values, are included in the figure legends. For all quantifications, the statistical significance immediately above the bars is with respect to the control genotype for that experimental group.

Results

Generation of *dMegf8* null mutants

The primary amino acid sequence of human MEGF8 protein revealed it as a transmembrane protein with a complex domain structure in its extracellular region, including CUB domains, multiple EGF repeats, KELCH domains, and laminin-EGF-like domains (Twigg et al., 2012). The mouse Megf8 protein also revealed a conserved domain structure similar to the human MEGF8 (Engelhard et al., 2013). The *Drosophila* Megf8, referred as dMegf8 (Lloyd et al., 2018), also revealed a complex domain structure with similar domains as the vertebrate Megf8 with some variations, but is the closest homolog of the vertebrate Megf8 family (Fig. 1*A*). dMegf8 shares >2400 amino acid sequence homology with human MEGF8 and close to 33% amino acid identity (Lloyd et al., 2018). In our studies, the *dMegf8* locus was identified in an ethyl methane sulfonate chemical mutagenesis screen that was designed to

uncover behavioral mutants with motor coordination deficits (A.V. and M.A.B., unpublished data). To explore the *in vivo* functions of dMegf8, and whether it has a role in neuronal and synaptic functions, we proceeded to generate a *dMegf8* null allele. The *dMegf8* locus (Fig. 1*B*) is composed of 6 exons with the ATG codon in exon 1 and the termination codon in exon 6. We used the *CRISPR-Cas9* gene editing strategy (Zhang et al., 2014) and inserted a *GFP* cassette to replace ~4062 bp starting from nucleotide sequence 5′-AAGCTATGGGGTCTG-3′ in exon 3 and ending in nucleotide sequence 5′-GATCGAAT GCCTCTT-3′ in exon 4 (for details, see Fig. 1*B*). We conducted PCR amplification using fly genomic DNA with a primer combination that distinguished the WT allele (primers 1 + 2 = 407 bp) (Fig. 1*B*,*C*) from the *dMegf8* mutant allele (primers 1 + 3 = 505 bp) (Fig. 1*B*,*D*). The PCR amplification confirmed the deletion of the sequences, and this *dMegf8* allele is referred as $dMegf8^{HSC}$. Next, we generated polyclonal antibodies against dMegf8 polypeptide to determine the relative molecular weight of dMegf8 and also to establish that $dMegf8^{HSC}$ is indeed a protein null allele. We also generated *UAS-dMegf8* transgenic flies to express dMegf8 using cell-specific *Gal4* drivers. We performed immunoblot analysis of adult head lysates from WT (+/+), $dMegf8^{HSC}$ and *elav-Gal4;UAS-dMegf8 (elav>dMegf8)* using anti-dMegf8 antibodies. As shown in Figure 1*E*, WT and *elav>dMegf8* lysates showed three major protein bands ranging from 250 to >300 kDa, which were absent from $dMegf8^{HSC}$ head lysates, confirming the specificity of the dMegf8 antibodies and $dMegf8^{HSC}$ as a protein null allele. Using pan-neuronal expression of *dMefg8* (*elav>dMegf8*), the dMegf8 protein is expressed at higher levels than in the WT control adult heads, indicating overexpression from the *dMegf8* transgene. The $dMegf8^{HSC}$ null allele reported here showed no significant embryonic lethality and only had <10% larva to adult lethality. We next assayed third instar larvae for various larval behavioral and coordination defects that included general motor activity using grid crossing assay (Fig. 1*F*), central zone release assay (Fig. 1*G*), peristalsis assay which analyses the muscle contraction waves (Fig. 1*H*), and larval righting assay (Fig. 1*I*). In all these assays, $dMegf8^{HSC}$ larvae showed significant deficits compared with WT control larvae. We also conducted adult locomotor assay that uses negative geotaxis (Gargano et al., 2005), as part of motor coordination and climbing activity. $dMegf8^{HSC}$ adult flies showed a significant weakness in their climbing activity, which declined progressively as flies aged (Fig. 1*J*), indicating that loss of dMegf8 leads to severe motor deficits in third instar larvae as well as adults. Another *dMegf8* null allele ($dMegf8^{\Delta 8}$) was reported previously, which showed larval lethality with denticle belt formation defects (Lloyd et al., 2018). It is not known whether variable genetic background contributes to early developmental lethality or whether there are any second site mutations associated with the $dMegf8^{\Delta 8}$ allele (Lloyd et al., 2018). Together, these data show that $dMegf8^{HSC}$ is indeed a null allele that is viable and that loss of dMegf8 is associated with severe motor deficits in both the larvae and adult flies.

dMegf8 localizes to synaptic terminals and is required for synaptic growth

Since mutations in human *MEGF8* have been associated with developmental malformations (Twigg et al., 2012; Pan et al., 2014; Giacopuzzi et al., 2017), and the murine *Megf8* null allele showed developmental malformations and embryonic lethality (Engelhard et al., 2013), we wanted to examine where dMegf8 was expressed and whether loss of dMegf8 had any consequences on synaptic development at the NMJ, as these synapses are generally considered to have a functional relevance to mammalian glutamatergic central synapses (Ruiz-Canada and Budnik, 2006; Xue et al., 2009). We first examined the endogenous expression of dMegf8 at the third instar larval NMJs by performing immunostaining for dMegf8 in combination with antibodies against the presynaptic active zone protein, Bruchpilot (Brp). We found that dMegf8 localized to the larval NMJ synapses in WT (Fig. 2*A*-*A*′′) when labeled with anti-dMegf8 (Fig. 2*A*,*A*′′) with respect to Brp (Fig. 2*A*′,*A*′′) (Wagh et al., 2006; Weyhersmuller et al., 2011). dMegf8 was not detected in the larval NMJ synapses in $dMegf8^{HSC}$ mutants (Fig. 2*B*,*B*′′), which were clearly highlighted by Brp immunostaining (Fig. 2*B*′,*B*′′), indicating that dMegf8 localizes to larval NMJ synapses. We next investigated the consequences of dMegf8 loss on the NMJ synaptic growth. We immunostained the larval NMJ of specified genotypes, including several alleles of *dMegf8* ($dMegf8^{F1}$ -from the ethyl methane sulfonate screen, $dMegf8^{HSC}$, and $dMegf8^{\Delta 8}$; Fig. 2*C*–*K*) (Lloyd et al., 2018) using anti-Hrp (green, Fig. 2*C*–*J*) to label neuronal membranes and anti-Discs large (Dlg) (red, Fig. 2*C*–*J*) to label Type I boutons (Lahey et al., 1994; Budnik et al., 1996). Compared with WT (Fig. 2*C*, quantified in Fig. 2*K*), all *dMegf8* mutant alleles showed synaptic undergrowth with fewer boutons (Fig. 2*D*–*F*,*K*). $dMegf8^{F1}$ also showed reduced synaptic growth comparable to $dMegf8^{HSC}$ (Fig. 2*D*,*K*). To ensure the $dMegf8^{HSC}$ homozygous phenotype was not caused by any other mutations in *cis*, we analyzed the $dMegf8^{HSC}$ allele over a deficiency chromosome (*Df(2L)7147*) that uncovered the *dMegf8* locus. Mutant larvae of $dMegf8^{HSC}/Df(2L)7147$ revealed NMJ growth phenotype that was not significantly different from $dMegf8^{HSC}/dMegf8^{HSC}$ homozygous mutants (data not shown), indicating that $dMegf8^{HSC}$ allele can be used for NMJ phenotypes in a homozygous state. While the $dMegf8^{HSC}$ homozygous null flies were viable and fertile, an independently generated *dMegf8* allele, also thought to be null, was reported to be larval lethal (Lloyd et al., 2018). We used one of the reported *dMegf8* mutant alleles, $dMegf8^{\Delta 8}$ (Lloyd et al., 2018), to analyze the synaptic growth in trans-allelic combination with $dMegf8^{HSC}$. $dMegf8^{HSC}/dMegf8^{\Delta 8}$ larvae showed similar synaptic undergrowth as the $dMegf8^{HSC}$ homozygous null mutants (Fig. 2*F*,*K*). Since $dMegf8^{\Delta 8}$ allele was also generated using *CRISPR/Cas9* deletion, it remains to be determined whether there is a second site mutation associated with this allele. Together, these data show that dMegf8 is expressed at the larval NMJ and that loss of dMegf8 causes a significant reduction in bouton growth at the NMJ.

On the contrary, presynaptic expression of dMegf8 in *elav>dMegf8* larvae led to increased growth of synaptic boutons (Fig. 2*G*,*K*), suggesting that dMegf8 overexpression caused enhanced bouton growth at the NMJ. Next, we wanted to assess whether the reduced synaptic growth seen in $dMegf8^{HSC}$ mutants could be rescued by presynaptic or postsynaptic expression of dMegf8. We found that presynaptic expression of dMegf8 in $dMegf8^{HSC}$ mutants ($dMegf8^{HSC/HSC}$; *elav-Gal4/UAS-dMegf8*) restored synaptic growth to WT levels (Fig. 2*H*,*K*); however, the postsynaptic expression of dMegf8 using *MHC-Gal4* (*MHC>dMegf8*) (Fig. 2*I*,*K*) did not show any changes in synaptic bouton growth compared with WT (Fig. 2*C*,*K*). The postsynaptic expression of dMegf8 in $dMegf8^{HSC}$ mutants ($dMegf8^{HSC/HSC}$; *MHC-Gal4>dMegf8*) failed to rescue the reduced bouton growth in $dMegf8^{HSC}$ mutants (Fig. 2*I*,*K*).

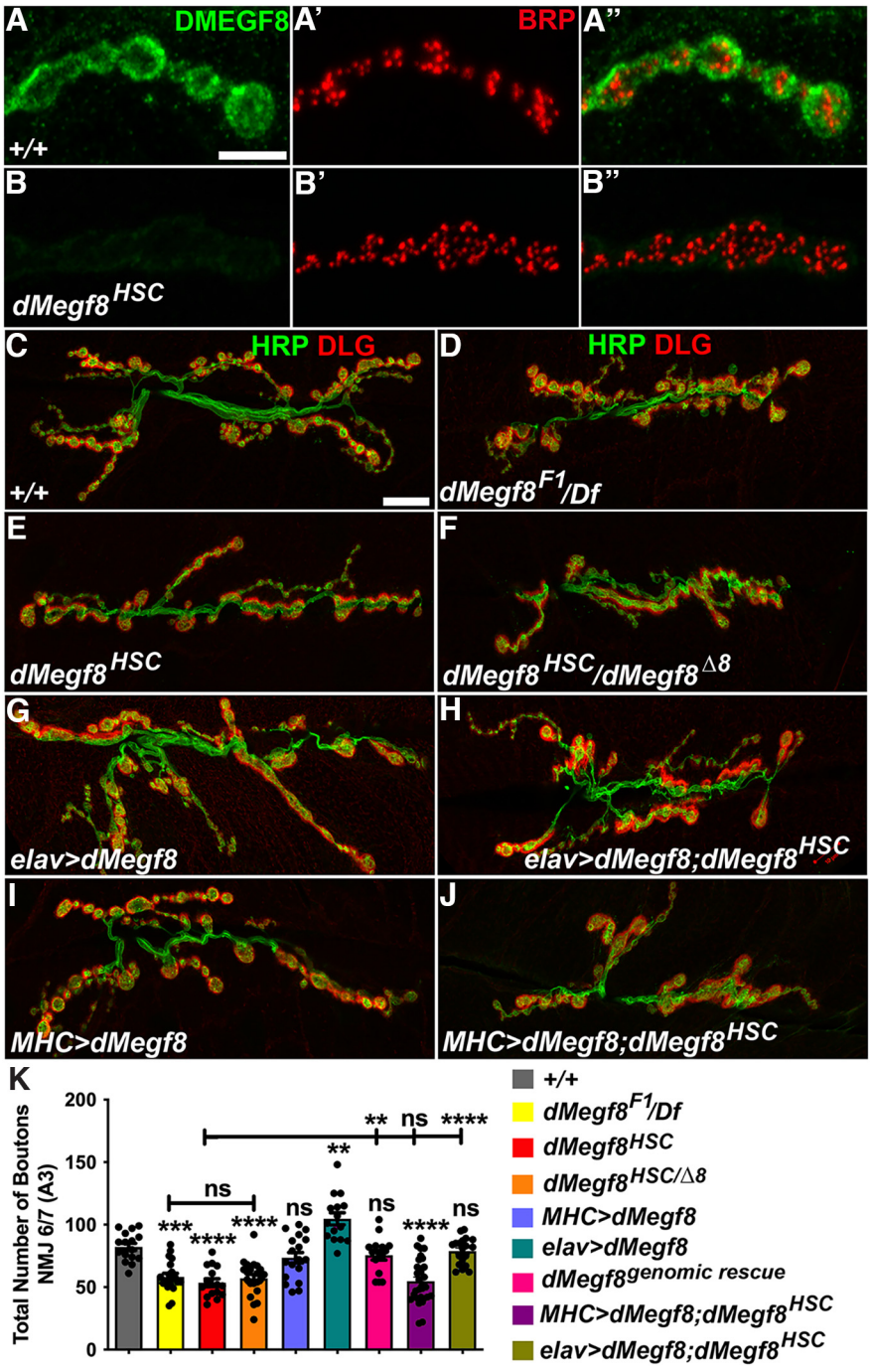

Figure 2. dMegf8 is expressed in synaptic terminals and required for synaptic bouton growth. ***A–B′′***, Confocal images in (***A***) +/+ and (***B***) *dMegf8*^{HSC} mutant third instar larvae NMJ Type Ib boutons at muscles 6/7 labeled with anti-dMegf8 (green) and anti-Brp (red). ***C–J***, Confocal images in (***C***) *dMegf8*^{HSC}, (***D***) *dMegf8* point mutant *dMegf8*^{F1}*/Df*, (***E***) *dMegf8* null mutant (*dMegf8*^{HSC}), (***F***) *dMegf8*^{HSC}*/dMegf8*$^{\Delta 8}$ trans-allelic combination, (***G***) presynaptic overexpression of *dMegf8* (*elav>dMegf8*), (***H***) presynaptic rescue (*elav>dMegf8;dMegf8*^{HSC}), (***I***) postsynaptic overexpression of dMegf8 (*MHC>dMegf8*), and (***J***) postsynaptic rescue (*MHC>dMegf8;dMegf8*^{HSC}) third instar larvae NMJ at muscles 6/7 labeled with the presynaptic marker Hrp (green) and the postsynaptic marker Dlg (red). ***K***, Quantification of total bouton numbers in indicated genotypes. ***K***, Data are mean ± SEM (one-way ANOVA test with Tukey's multiple comparisons): $F_{(8,160)} = 22.3064$, +/+ versus *F1/Df*: ***$p = 0.0001$, +/+ versus *dMegf8*^{HSC}: ****$p < 0.0001$, +/+ versus *dMegf8*^{HSC}*/*$^{\Delta 8}$: ****$p < 0.0001$, +/+ versus *MHC>dMegf8*: $p = 0.7496$, +/+ versus *elav>dMegf8*: **$p = 0.0014$, +/+ versus Genomic Rescue: $p = 0.9467$, +/+ versus *MHC>dMegf8; dMegf8*^{HSC}: ****$p < 0.0001$, +/+ versus *elav>dMegf8; dMegf8*^{HSC}: $p = 0.9992$, *dMegf8*^{HSC} versus *F1/Df*: $p = 0.9915$, *dMegf8*^{HSC} versus *dMegf8*^{HSC}*/*$^{\Delta 8}$: $p = 0.9989$, *dMegf8*^{HSC} versus genomic Rescue: **$p = 0.0027$, *dMegf8*^{HSC} versus *MHC>dMegf8; dMegf8*^{HSC}: $p > 0.9999$, *dMegf8*^{HSC} versus *elav>dMegf8; dMegf8*^{HSC}: ****$p < 0.0001$. Scale bars: ***A–B′′***, 5 μm; ***C–J***, 20 μm.

These data show that presynaptic dMegf8 expression is able to promote synaptic growth at NMJ and that the synaptic growth function of dMegf8 is mostly presynaptic as the postsynaptic expression neither promoted nor rescued the synaptic growth at the NMJ.

Loss of dMegf8 affects the distribution of presynaptic and postsynaptic proteins

Since NMJ bouton growth was affected in *dMegf8* mutants, we wanted to determine whether loss of dMegf8 would have any consequences on the proper assembly of presynaptic and postsynaptic proteins which display a stereotypic localization at the NMJ synapses with respect to assembly and distribution. We first studied the localization of the well-characterized active zone protein, Brp (Wagh et al., 2006) (green, Fig. 3*A*, *A′′*; Fig. 3*B*, *B′′*) with respect to the postsynaptic glutamate receptor subunit, GluRIIA (Marrus et al., 2004) (red, Fig. 3*A′*,*A′′*; Fig. 3*B′*,*B′′*) in WT (Fig. 3*A*-*A′′*) and *dMegf8*^{HSC} mutant (Fig. 3*B′*,*B′′*) larval NMJ. In WT larvae (Fig. 3*A*–*A′′*), active zones labeled with anti-Brp (Fig. 3*A*,*A′′*) were juxtaposed to the GluRIIA punctae (Fig. 3*A′*, *A′′*), which was similar in *dMegf8*^{HSC} mutant synapses (Fig. 3*B*-*B′′*), indicating that the alignment of the presynaptic BRP and postsynaptic GluRIIA was not significantly affected. Next, we analyzed the number of Brp puncta in the WT (Fig. 3*A*-*A′′*) and *dMegf8*^{HSC} mutants (Fig. 3*B*-*B′′*) to determine whether there were any differences in the number of active zones per bouton area. *dMegf8*^{HSC} mutants showed a significant increase in the number of Brp-positive puncta as quantified and normalized to the bouton area in *dMegf8*^{HSC} mutants compared with WT (Fig. 3*C*). GluRIIA puncta also showed similar increase as the Brp puncta in *dMegf8* mutants compared with the WT (data not shown). These data indicate that there is increase in the number of Brp-positive active zones in *dMegf8*^{HSC} mutant NMJ synapses.

Next, we determined whether *dMegf8*^{HSC} mutants caused any aberrations in the organization or differentiation of postsynaptic specializations. We studied the localization of Discs large (Dlg, red, Fig. 3*D*–*E′*), which has been shown to function both presynaptically and postsynaptically in the proper assembly of the subsynaptic reticulum (SSR) in Type Ib boutons (Lahey et al., 1994; Budnik et al., 1996) together with the neuronal membrane marker, Hrp (green, Fig. 3*D′*, *E′*). In WT (Fig. 3*D*,*D′*), Dlg localization is typically in the periphery of the bouton

circumference and mostly excluded from the core of the boutons. However, in *dMegf8*^{HSC} mutants (Fig. 3*E*,*E*′), there was a more diffuse Dlg distribution throughout the bouton; and there was no clear separation in the presynaptic Hrp areas, as is observed in the WT boutons (Fig. 3*D*,*D*′), suggesting that loss of dMegf8 affected the localization of Dlg at the NMJ. Next, we tested whether the mislocalization of Dlg in the *dMegf8*^{HSC} mutant boutons would be rescued by presynaptic or postsynaptic expression of dMegf8. As shown in Figure 3*F* and at a higher magnification in Figure 3*F*′, *elav>dMegf8;dMegf8*^{HSC} NMJs showed improved Dlg localization that was more in the bouton perimeter similar to the WT boutons (Fig. 3*D*) than that displayed by *MHC>dMegf8;dMegf8*^{HSC} NMJs (Fig. 3*G*, higher magnification in Fig. 3*G*′), indicating that presynaptic expression of dMegf8 restored Dlg localization better than the postsynaptic dMegf8 expression. Together, these data show that dMegf8 is required for proper presynaptic and postsynaptic protein assembly and distribution at the NMJs, and that presynaptic expression was able to restore Dlg localization at the NMJ compared with *dMegf8*^{HSC} mutants.

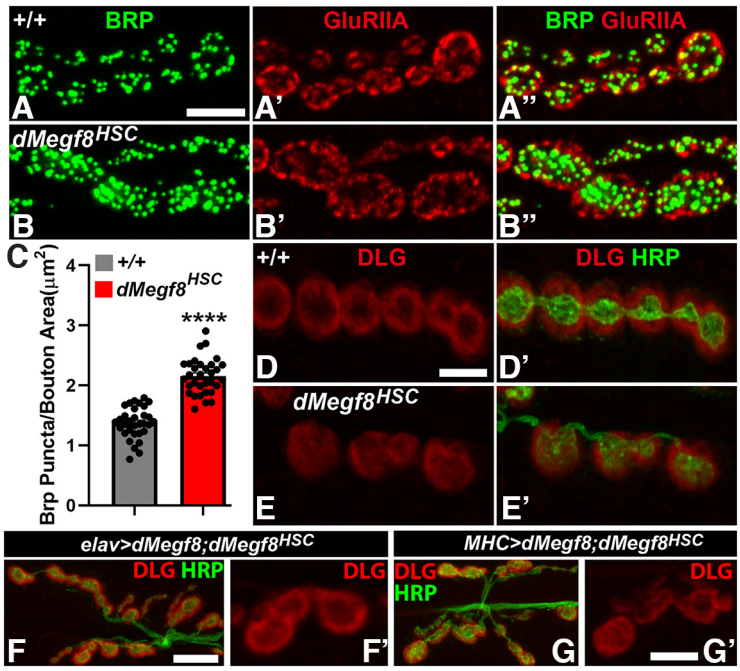

Figure 3. *dMegf8*^{HSC} mutants show altered localization of presynaptic/postsynaptic proteins. ***A–B″***, Confocal images in (***A***) +/+ and (***B***) *dMegf8*^{HSC} mutant third instar larval NMJ Type Ib boutons at muscles 6/7 labeled with the presynaptic protein Brp (green) and the postsynaptic protein GluRIIA (red). ***C***, Quantification of Brp puncta/bouton area (μm^2) in WT and *dMegf8*^{HSC} mutants. ***D–E′***, Confocal images in (***D***) +/+ and (***E***) *dMegf8*^{HSC} mutant third instar larvae NMJ labeled with the presynaptic marker Hrp (green) and the postsynaptic protein Dlg (red). ***C***, Quantification data are mean ± SEM; $t_{(62)} = 11.14$. ****$p < 0.0001$ (unpaired Student's *t* test). ***F–G′***, Dlg localization in *dMegf8*^{HSC} mutants that have either presynaptic expression (*elav>dMegf8*) (***F***,***F′***) or postsynaptic expression (*MHC>dMegf8*) (***G–G′***). Scale bars: ***A–B′***, ***F***, ***G***, 5 μm; ***D–E′***, ***F′***, ***G′***, 20 μm.

Presynaptic and postsynaptic ultrastructural abnormalities in *dMegf8* mutants

The reduced synaptic growth and altered subcellular localization of Dlg observed in *dMegf8* mutants led us to analyze the ultrastructure of the synaptic boutons in these mutants to examine the organization of the overall synaptic architecture and how that compared with WT controls. The WT boutons are characterized by morphologically distinct and closely apposed presynaptic and postsynaptic membranes (Fig. 4*A*). The presynaptic compartment also contains synaptic vesicles, apart from organelles, such as mitochondria. The presynaptic membrane has active zones that are composed of electron dense structures called T-bars (Fig. 4*A*) (Wagh et al., 2006). The Type Ib boutons at the postsynaptic muscle are surrounded by elaborate membrane invaginations, the SSR, which occupies a large area on the postsynaptic side (Fig. 4*A*,*B*) (Budnik et al., 1996; Jia et al., 1993). We performed serial sectioning of boutons from WT, *dMegf8*^{F1}, and *dMegf8*^{HSC} mutants and subjected them to morphometric analyses to determine any presynaptic and/or postsynaptic defects. In addition, we also assessed whether any of the synaptic defects displayed by *dMegf8*^{HSC} mutants would be rescued by expressing dMegf8 either presynaptically or postsynaptically.

We did not observe any significant changes in the overall area of the boutons in *dMegf8*^{HSC} (Fig. 4*B*, quantified in Fig. 4*F*) and *dMegf8*^{F1} mutants (Fig. 4*C*,*F*) compared with WT (Fig. 4*A*,*F*) or any of the other genotypes analyzed (Fig. 4*D–F*). It is important to note that, although many d*Megf8*^{HSC} mutant boutons had larger bouton areas, there was also a significant variability. The number of active zones (arrows) and total PSD length (arrowheads) showed a significant increase in *dMegf8*^{HSC} (Fig. 4*B*, quantified in Fig. 4*G* and Fig. 4*H*, respectively) and *dMegf8*^{F1} mutants (Fig. 4*C*,*G*,*H*) compared with WT controls (Fig. 4*A*,*G*, *H*). Both increased active zone numbers and total PSD length in *dMegf8*^{HSC} mutants were rescued to WT levels in the presynaptic rescue as seen in *elav>dMegf8;dMegf8*^{HSC} (Fig. 4*D*, *G*,*H*), while the postsynaptic expression of *dMegf8* in *dMegf8*^{HSC} mutants, as seen in *MHC>dMegf8;dMegf8*^{HSC} (Fig. 4*E*,*G*,*H*), did not show any changes in these parameters compared with *dMegf8*^{HSC} mutants (Fig. 4*B*,*G*,*H*). Postsynaptic SSR morphology was severely compromised in *dMegf8*^{HSC} (Fig. 4*B*, *B*′) and *dMegf8*^{F1} (Fig. 4*C*,*C*′) with thinner folds compared with WT controls (Fig. 4*A*,*A*′). Morphometric analysis of normalized SSR width (Fig. 4*I*) showed a significant reduction in *dMegf8*^{HSC} mutants compared with WT controls (Fig. 4*I*). *dMegf8*^{F1} mutants also showed reduced normalized SSR width (Fig. 4*I*). Interestingly, reduction in the normalized SSR width was fully rescued when dMegf8 was expressed postsynaptically in *dMegf8*^{HSC} mutants as seen in *MHC>dMegf8;dMegf8*^{HSC} (Fig. 4*I*) but not by the presynaptic expression of dMefg8 as observed in *elav>dMegf8; dMegf8* ^{HSC} (Fig. 4*I*). Together, the EM and morphometric analyses indicate that loss of dMegf8 leads to defective ultrastructural organization of both the presynaptic and postsynaptic areas at the NMJ and that dMegf8 functions both presynaptically and postsynaptically to organize the proper synaptic apparatus.

Synaptic transmission is reduced in *dMegf8* mutants

As shown in the preceding sections, loss of dMegf8 results in reduced synaptic growth at the larval NMJ (Fig. 2) and causes ultrastructural abnormalities at the synapse (Fig. 4). We next examined the consequences of loss of dMegf8 on synaptic transmission at the NMJs, as well as whether presynaptic or postsynaptic expression of dMegf8 in *dMegf8* mutants will restore the synaptic transmission in *dMegf8* mutants. We performed electrophysiological analyses on muscle 6 of third-instar larval

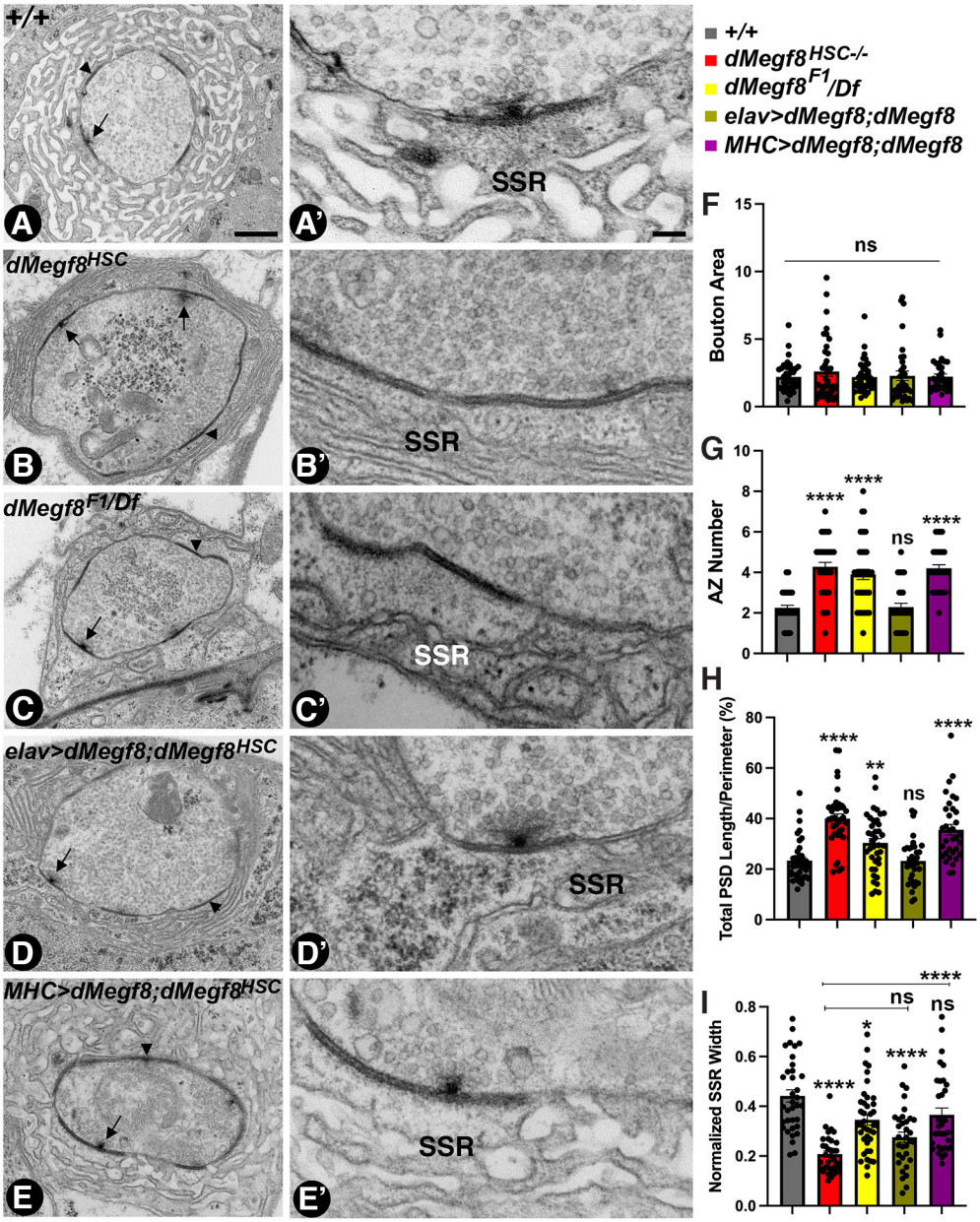

Figure 4. Loss of dMegf8 causes synaptic ultrastructural defects. ***A–E′***, TEM images of cross sections through Type Ib boutons in (***A***) +/+, (***B***) *dMegf8*^{HSC} mutant, (***C***) *dMegf8* point mutant *dMegf8*^{F1}*/Df*, (***D***) presynaptic rescue (*elav>dMegf8;dMegf8*^{HSC}), and (***E***) postsynaptic rescue (*MHC>dMegf8;dMegf8*^{HSC}) at low magnification (***A–E***) and high magnification (***A′–E′***). Arrows indicate the active zones (AZs). Arrowheads indicate the PSDs in ***A–E***. ***F–I***, Quantification in (***F***) total bouton area, (***G***) number of AZs, (***H***) total PSD length/perimeter (%), and (***I***) normalized SSR width in represented genotypes. ***F–I***, Data are mean ± SEM (one-way ANOVA test with Tukey's multiple comparisons). ***F***, $F_{(4,183)} = 0.4529$, +/+ versus *dMegf8*^{HSC}: $p = 0.7990$, +/+ versus *F1/Df*: $p > 0.9999$, +/+ versus *elav>dMegf8; dMegf8*^{HSC}: $p = 0.9994$, +/+ versus *MHC>dMegf8; dMegf8*^{HSC}: $p > 0.9999$. ***G***, $F_{(4.000,159.4)} = 25.97$, +/+ versus *dMegf8*^{HSC}: ****$p < 0.0001$, +/+ versus *F1/Df*: ****$p < 0.0001$, +/+ versus *elav>dMegf8; dMegf8*^{HSC}: $p = 0.9999$, +/+ versus *MHC>dMegf8; dMegf8*^{HSC}: ****$p < 0.0001$ (Brown-Forsythe and Welch ANOVA with Games-Howell's multiple comparisons specifically). ***H***, $F_{(4,179)} = 18.18$, +/+ versus *dMegf8*^{HSC}: ****$p < 0.0001$, +/+ versus *F1/Df*: *$p = 0.0292$, +/+ versus *elav>dMegf8; dMegf8*^{HSC}: $p > 0.9999$, +/+ versus *MHC>dMegf8; dMegf8*^{HSC}: ****$p < 0.0001$. ***I***, $F_{(4,169)} = 16.03$, +/+ versus *dMegf8*^{HSC}: ****$p < 0.0001$, +/+ versus *F1/Df*: *$p = 0.0136$, +/+ versus *elav>dMegf8; dMegf8*^{HSC}: ****$p < 0.0001$, +/+ versus *MHC>dMegf8; dMegf8*^{HSC}: $p = 0.1136$, *dMegf8*^{HSC} versus *elav>dMegf8; dMegf8*^{HSC}: $p = 0.2102$, *dMegf8*^{HSC} versus *MHC>dMegf8; dMegf8*^{HSC}: ****$p < 0.0001$. Scale bars: ***A–E***, 600 nm; ***A′–E′***, 200 nm.

body walls of all relevant genotypes and recorded the EJPs in 0.5 mM $[Ca^{2+}]_o$ at 0.2 Hz under identical conditions (Feeney et al., 1998; Shi et al., 2019). Representative EJP graphs from the control (*wCS*) (Fig. 5*A*), *dMegf8*^{HSC} mutants (Fig. 5*B*), presynaptic dMegf8 expression in *elav>dMegf8;dMegf8*^{HSC} mutants (Fig. 5*C*), and postsynaptic dMegf8 expression in *MHC>dMegf8; dMegf8*^{HSC} mutants (Fig. 5*D*). *dMegf8*^{HSC} mutants exhibited a reduction in EJP amplitude (Fig. 5*B*, quantified in Fig. 5*E*). The presynaptic expression of dMegf8 was able to fully rescue the EJP amplitude of *dMegf8*^{HSC} mutants (Fig. 5*C*,*E*), whereas the postsynaptic dMegf8 expression did not rescue the EJP amplitude in *dMegf8*^{HSC} mutants (Fig. 5*D*,*E*). Interestingly, the mEJP amplitudes did not show any significant differences in *dMegf8*^{HSC} mutants, in *elav>dMegf8;dMegf8*^{HSC} mutants and in *MHC>dMegf8;dMegf8*^{HSC} mutants compared with *wCS* controls, suggesting that the synaptic vesicle contents were not altered by loss of dMegf8 (Fig. 5*F*). *dMegf8*^{HSC} mutants and postsynaptic dMegf8 expression in *MHC>dMegf8;dMegf8*^{HSC}

mutants revealed severely decreased quantal contents compared with *wCS* controls, and the presynaptic dMegf8 expression in *elav>dMegf8;dMegf8*^{HSC} mutants was similar to *wCS* controls (Fig. 5*G*). The paired pulse ratio (Fig. 5*H*) and the mEJP frequency (Fig. 5*I*) in *dMegf8*^{HSC} mutants, presynaptic dMegf8 expression in *elav>dMegf8;dMegf8*^{HSC} mutants and postsynaptic dMegf8 expression in *MHC>dMegf8;dMegf8*^{HSC} mutants did not show any significant differences compared with *wCS* controls. Together, our data show that dMegf8 functions presynaptically for synaptic transmission at the NMJs.

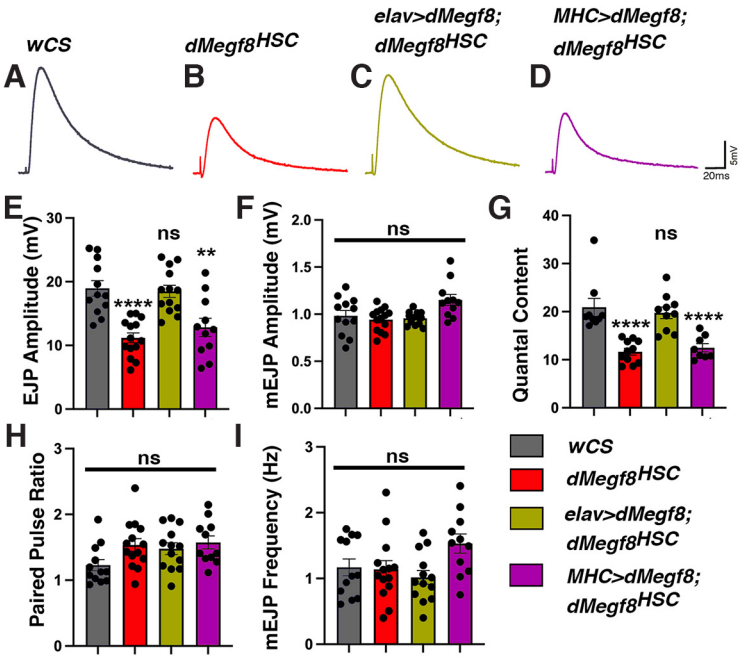

Figure 5. dMegf8 is required for proper synaptic transmission. ***A–D***, Representative electrophysiological traces showing EJPs from (***A***) WT (*wCS*), (***B***) *dMegf8*^{HSC} mutant, (***C***) presynaptic rescue (*elav>dMegf8;dMegf8*^{HSC}), and (***D***) postsynaptic rescue (*MHC>dMegf8;dMegf8*^{HSC}). ***E–I***, Quantification of (***E***) EJP amplitude, (***F***) mEJP amplitude, (***G***) quantal contents, (***H***) paired pulse ratio, and (***I***) mEJP frequency in respective genotypes. ***E–I***, Data are mean ± SEM (one-way ANOVA test with Tukey's multiple comparisons). ***E***, $F_{(4,58)} = 11.53$, +/+ versus *dMegf8*^{HSC}: ****$p < 0.0001$, +/+ versus *elav>dMegf8; dMegf8*^{HSC}: $p = 0.9980$, +/+ versus *MHC>dMegf8; dMegf8*^{HSC}: **$p = 0.0026$. ***F***, $F_{(4,58)} = 4.311$, +/+ versus *dMegf8*^{HSC}: $p = 0.9658$, +/+ versus *elav>dMegf8; dMegf8*^{HSC}: $p = 0.9936$, +/+ versus *MHC>dMegf8; dMegf8*^{HSC}: $p = 0.0861$. ***G***, $F_{(4,43)} = 13.95$, +/+ versus *dMegf8*^{HSC}: ****$p < 0.0001$, +/+ versus *elav>dMegf8; dMegf8*^{HSC}: $p = 0.9503$, +/+ versus *MHC>dMegf8; dMegf8*^{HSC}: ****$p < 0.0001$. ***H***, $F_{(4,58)} = 3.195$, +/+ versus *dMegf8*^{HSC}: $p = 0.1143$, +/+ versus *elav>dMegf8; dMegf8*^{HSC}: $p = 0.2908$, +/+ versus *MHC>dMegf8; dMegf8*^{HSC}: $p = 0.0800$. ***I***, $F_{(4,58)} = 6.865$, +/+ versus *dMegf8*^{HSC}: $p = 0.9998$, +/+ versus *elav>dMegf8; dMegf8*^{HSC}: $p = 0.9088$, +/+ versus *MHC>dMegf8; dMegf8*^{HSC}: $p = 0.2920$.

Synaptic proteins regulating NMJ growth and structure show reduced expression in *dMegf8* mutants

Since dMegf8 is a transmembrane protein and *dMegf8* mutants display synaptic growth defects as well as deficits in synaptic ultrastructure and synaptic transmission, we next wanted to examine whether dMegf8 has any association or interactions with proteins that regulate synaptic growth and architecture. Synaptic transmembrane proteins are critical for trans-synaptic adhesion and signaling for proper synaptic organization and function (Sun and Xie, 2012; Banerjee et al., 2017; Banerjee and Riordan, 2018). Since most phenotypes of *dMegf8*^{HSC} mutants were rescued presynaptically, dMegf8 likely functions in association with other presynaptic proteins to coordinate synaptic growth and organization. Two key proteins in the synaptic machinery that are well known in regulating synaptic growth, organization, and function are the trans-membrane proteins, Drosophila neurexin (Dnrx) (Li et al., 2007; Zeng et al., 2007) and the Type II receptor of the BMP signaling pathway wishful thinking (wit) (Aberle et al., 2002; McCabe et al., 2003; Banerjee et al., 2017; Banerjee and Riordan, 2018; Guangming et al., 2020). We next set out to investigate whether dMegf8 coordinates synaptic growth with Dnrx and/or Wit and might be part of a synaptic membrane protein complex. We first wanted to test whether the endogenous dMegf8 localization was affected in larval NMJ of *dnrx* and *wit* mutants. Similar to data presented in Figure 2, endogenous dMegf8 (green, Fig. 6*A-D″*) localized to the NMJ synaptic terminals in WT (Fig. 6*A*,*A″*) and absent in *dMegf8*^{HSC} mutants (Fig. 6*B*,*B″*). Compared with the WT dMegf8 localization (Fig. 6*A*, *A″*), the dMegf8 localization in *dnrx* (Fig. 6*C*,*C″*) and *wit* mutants (Fig. 6*D*,*D″*) was diffuse with a significant decrease in the fluorescence intensity levels in both *dnrx* and *wit* mutants (quantified in Fig. 6*J*). Brp was used as a presynaptic marker (red, Fig. 6*A′*,*A″*,*B′*,*B″*,*C′*,*C″*,*D′*,*D″*). Next, we wanted to examine any alterations in the localization and/or fluorescence intensities of Dnrx and Wit in *dMegf8*^{HSC} mutants by immunolocalization of Dnrx in WT, *dMegf8*^{HSC} mutants, and *dnrx* mutants NMJs. We observed that Dnrx localization in *dMegf8*^{HSC} mutants (Fig. 6*F*,*F′*) was also significantly reduced compared with WT controls (Fig. 6*E*,*E′*, quantified in Fig. 6*K*). We also tested for Wit localization; however, the endogenous Wit levels in the larval NMJs were undetectable using standard immunohistochemistry protocols with anti-Wit antibodies as reported previously (Nahm et al., 2013; Banerjee et al., 2017). Therefore, to study Wit localization, we followed a strategy of overexpressing Wit presynaptically using the *elav-Gal4* driver in WT (*elav-Gal4; UAS-wit*, Fig. 6*H*,*H′*) and in *dMegf8*^{HSC} mutant background (*elav-Gal4/UAS-wit;dMegf8*^{HSC}, Fig. 6*I*,*I′*). The expression of Wit in *elav-Gal4;UAS-wit;dMegf8* NMJs (red, Fig. 6*I*,*I′*) was dramatically reduced compared with Wit expression in *elav-Gal4; UAS-wit* (red, Fig. 6*H*,*H′*, quantified in Fig. 6*L*) in the WT background. The immunolocalization and levels of Dnrx and Wit were not significantly different between *dMegf8*^{HSC}/*dMegf8*^{HSC} homozygous mutants compared with *dMegf8*$^{\Delta 8}$/*dMegf8*^{HSC} trans-allelic mutants (data not shown). Together, these data demonstrate that dMegf8 is necessary for the proper localization and clustering of presynaptic Dnrx and Wit, and that these proteins may be interdependent for their proper assembly at the NMJ synaptic terminals.

dMegf8 mutants show normal levels pMad and Trio, and *dMegf8* shows genetic interactions with *dnrx* and *wit*

Since Wit localization was significantly reduced by loss of dMegf8, we next determined whether any downstream effectors of the BMP signaling pathway would also get impacted by loss of dMegf8. At the *Drosophila* NMJ, BMP signaling is essential for synaptic growth and homeostasis (Bayat et al., 2011). In retrograde BMP signaling pathway, the ligand glass bottom boat

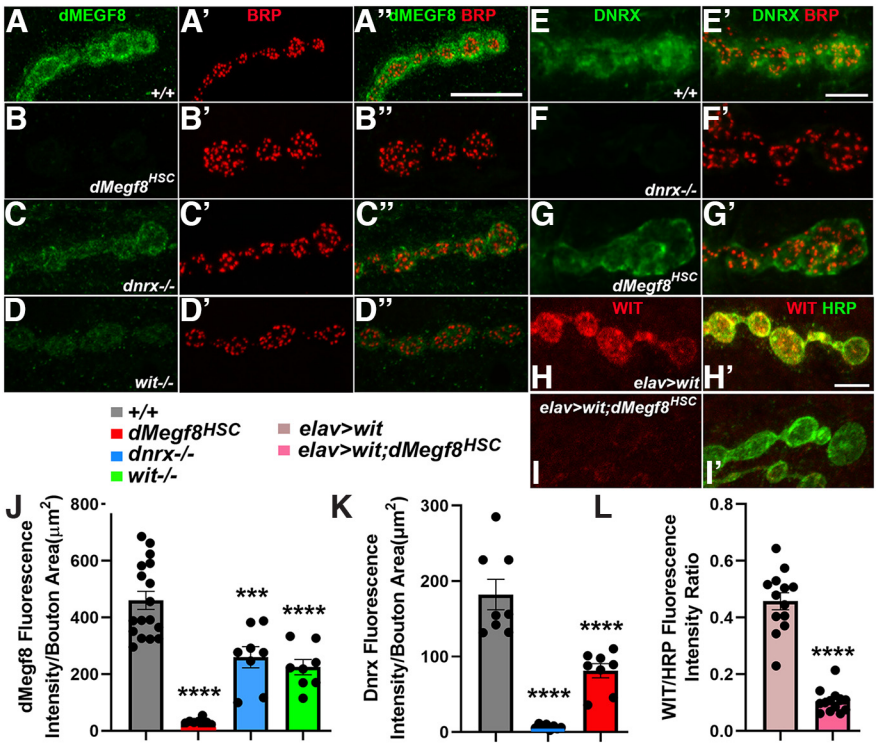

Figure 6. Interdependency of dMegf8, Dnrx, and Wit in their localization and stability. ***A–D′′***, Confocal images in (***A***) +/+, (***B***) *dMegf8*^{HSC} mutant, (***C***) *dnrx* mutant, and (***D***) *wit* mutant third instar larval NMJ labeled with anti-dMegf8 (green) and anti-Brp (red). ***E–G′***, Confocal images in (***E***) +/+, (***F***) *dnrx* mutant, and (***G***) *dMegf8*^{HSC} mutant third instar larval NMJ labeled with anti-Dnrx (green) and anti-Brp (red). ***H–I′***, Confocal images of (***H***) *elav>wit* and (***I***) *elav>wit; dMegf8*^{HSC} larval NMJ labeled with anti-Hrp (green) and anti-Wit (red). ***J***, Quantification of dMegf8 fluorescence intensity/bouton area in WT (+/+), *dMegf8*^{HSC}, *dnrx*, and *wit* mutants. Data are mean ± SEM; $F_{(7,37)} = 18.25$, +/+ versus *dMegf8*^{HSC}: ****$p < 0.0001$, +/+ versus *dnrx*$^{-/-}$: ***$p = 0.0005$, +/+ versus *wit*$^{-/-}$: ****$p < 0.0001$ (one-way ANOVA test with Tukey's multiple comparisons). ***K***, Quantification of Dnrx fluorescence intensity/bouton area in WT (+/+), *dnrx*, and *dMegf8*^{HSC} mutants. Data are mean ± SEM; $F_{(2,21)} = 46.54$, +/+ versus *dnrx*$^{-/-}$: ****$p < 0.0001$, +/+ versus *dMegf8*^{HSC}: ****$p < 0.0001$ (one-way ANOVA test with Tukey's multiple comparisons). ***L***, Quantification of Wit/Hrp fluorescence intensity ratio in *elav>wit* and *elav>wit; dMegf8*^{HSC} mutants. Data are mean ± SEM; $t_{(24)} = 11.02$, ****$p < 0.0001$ (unpaired Student's *t* test). Scale bars: ***A–D′′***, 10 μm; ***E–G′***, 5 μm; ***H–I′***, 5 μm.

(Gbb) from postsynaptic muscles binds to presynaptic Type I receptors Thickveins (Tkv), Saxophone (Sax), and Type II receptor Wit leading to increased phosphorylation of BMP transcription factor, Mothers against dpp (Mad), and its subsequent accumulation in the nucleus (Aberle et al., 2002; Marques et al., 2002; McCabe et al., 2003; Dudu et al., 2006; Ball et al., 2010). pMad binds directly to *Trio* promoter and enhance the transcription of *Trio*. Trio activates other downstream effectors in the neuronal soma or at the synapses leading to alterations in the actin cytoskeleton and regulating synaptic growth (Awasaki et al., 2000; Ball et al., 2010). Immunolabeling of NMJs with anti-pMad (PS-1, red) and Hrp (green) in WT (Fig. 7*A*,*A′*) and *dMegf8*^{HSC} mutants (Fig. 7*B*,*B′*) did not show any difference in fluorescence intensities of pMad (quantification in Fig. 7*E*). Similarly, pMad (SMAD, red) fluorescence levels in WT (Fig. 7*C*, quantified in Fig. 7*F*) and *dMegf8*^{HSC} mutant VNC (Fig. 7*D*, quantified in Fig. 7*F*) also did not show any significant differences. Total levels of pMad (Smad) analyzed by immunoblots (Fig. 7*G*, quantified in Fig. 7*I*) from VNC of WT and *dMegf8*^{HSC} mutants showed no significant difference while pMad levels in *wit* mutants showed severe reduction as reported previously (Fig. 7*G*,*I*) (Banerjee et al., 2017). Trio levels assessed by immunoblotting analysis of VNC also showed no significant difference between WT and *dMegf8*^{HSC} mutants (Fig. 7*H*, quantified in Fig. 7*J*). These data indicate that loss of dMegf8 does not impact the levels of downstream BMP effectors, pMad and Trio.

Given the interdependency of dMegf8, Dnrx, and Wit localization as shown in Figure 6 and a common synaptic undergrowth phenotype seen in *dMegf8*, *dnrx*, and *wit* mutants (Fig. 2) (Aberle et al., 2002; Marques et al., 2002; Li et al., 2007; Banerjee et al., 2017), we were interested in determining whether *dMegf8*, *dnrx*, and *wit* displayed any genetic interactions to coordinate synaptic growth. Thus, for our genetic interaction studies, we used the synaptic undergrowth as our phenotypic readout and generated various genetic combinations of *dMegf8* and *dnrx* as well as *dMegf8* and *wit* (Fig. 7*K–R*). First, we examined the synaptic growth of *dMegf8*$^{HSC+/-}$ (Fig. 7*K*,*S*) and *dnrx*$^{+/-}$ (Fig. 7*S*) heterozygotes compared with WT and found no significant differences (Fig. 7*S*). Next, we analyzed the double heterozygous combination of *dMegf8* $^{HSC+/-}$; *dnrx*$^{+/-}$ (Fig. 7*L*,*S*) and found a significant decrease in bouton numbers compared with the single heterozygotes of *dMegf8*$^{HSC+/-}$ and *dnrx*$^{+/-}$ (Fig. 7*S*). We further compared the bouton numbers in single mutants of *dMegf8* $^{HSC-/-}$ (Fig. 7*S*) and *dnrx*$^{-/-}$ (Fig. 7*M*,*S*) and found no significant differences between the two genotypes (Fig. 7*S*). Similarly, double mutants of *dMegf8* $^{HSC-/-}$; *dnrx*$^{-/-}$ (Fig. 7*N*,*S*) showed similar reduction in bouton growth compared with *dMegf8* $^{HSC-/-}$ or *dnrx*$^{-/-}$ single mutants (Fig. 7*S*). These data suggest that dMegf8 and Dnrx loss affects synaptic growth similarly and that they may function together in regulating NMJ synaptic growth.

We next tested genetic interactions between *dMegf8* and *wit* using a similar approach as presented above. NMJ bouton counts of *dMegf8* $^{HSC+/-}$ and *wit*$^{+/-}$ (Fig. 7*O*,*T*) showed no differences compared with WT (Fig. 7*T*), while the double heterozygous combination of *dMegf8* $^{HSC+/-}$;*wit*$^{+/-}$ (Fig. 7*P*, *T*) displayed a significant reduction. Next, the single mutants of *dMegf8*$^{HSC-/-}$ and *wit*$^{-/-}$ (Fig. 7*Q*,*T*) showed undergrowth phenotypes similar to *dMef8*$^{HSC-/-}$;*wit*$^{-/-}$ double mutants (Fig. 7*R*,*T*). These data indicate that *dMegf8* and *wit* display genetic interactions and are involved in coordinating synaptic growth at NMJ. Together, our data show that *dMegf8*, *dnrx*, and *wit* show genetic interactions and function in synaptic growth and organization at the NMJ synapses without severely impacting the BMP signaling pathway.

dMegf8, Dnrx and Wit function in a biochemical complex

Given that the dMegf8 fluorescence intensity was reduced in *dnrx* and *wit* mutants and the localization of Dnrx and Wit was also affected in *dMegf8* mutants, we wanted to examine the total levels of these proteins in the mutant backgrounds of one another (Fig. 8). In addition, since *dMegf8* displayed genetic interactions with *dnrx* and *wit*, we also wanted to determine

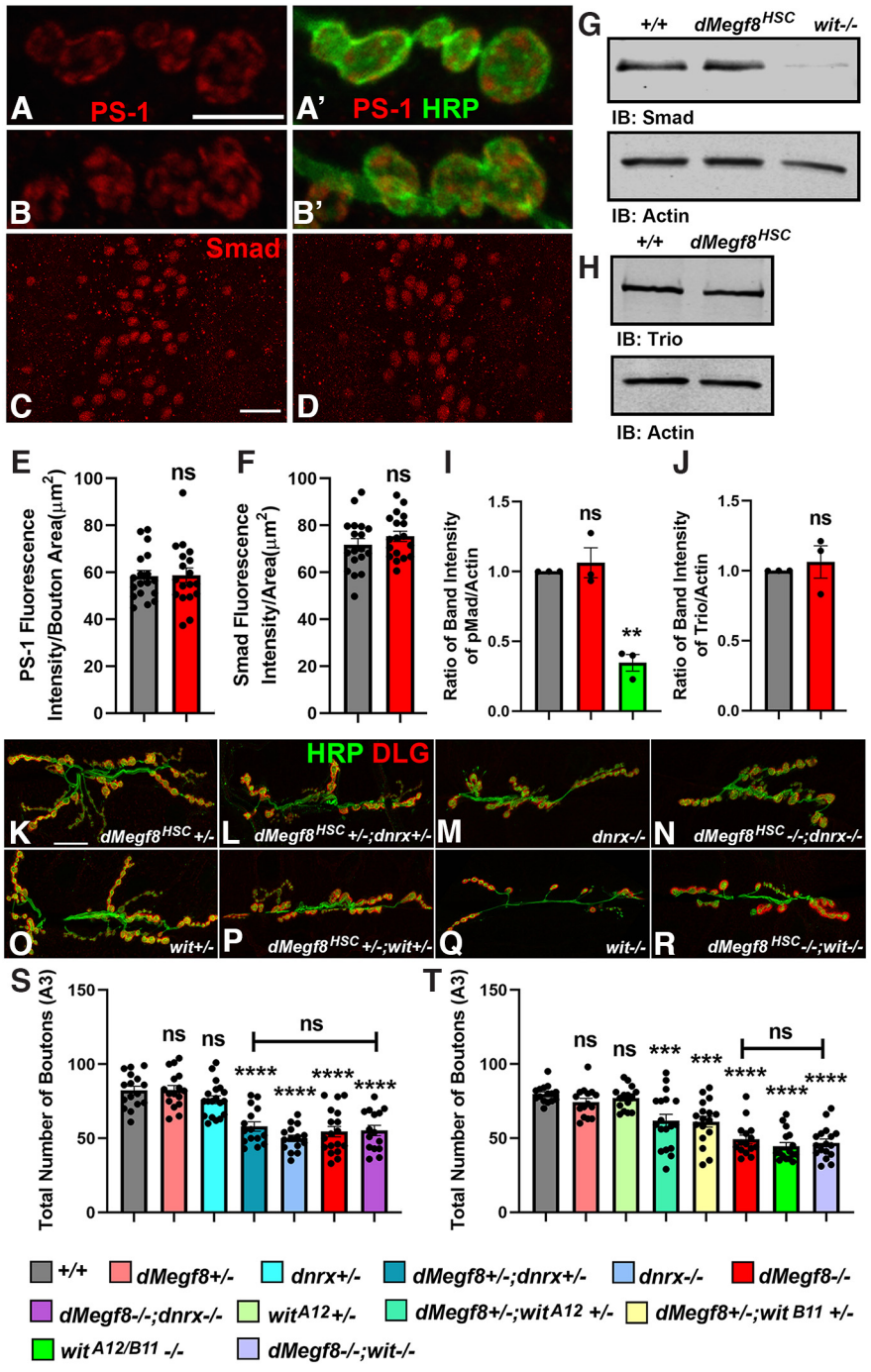

Figure 7. BMP downstream effectors in *dMegf8* mutants and genetic interactions between *dMegf8, dnrx*, and *wit*. ***A–B'***, Confocal images in (***A***) +/+ and (***B***) $dMegf8^{HSC}$ mutant third instar larval NMJ labeled with anti-PS-1 (red) and anti-Hrp (green). ***C***, ***D***, Confocal images of (***C***) +/+ and (***D***) $dMegf8^{HSC}$ mutant larval VNC labeled with anti-Smad (red). ***E***, Quantification of PS-1 fluorescence intensity/bouton area in the specified genotypes in ***A***, ***B***. Data are mean ± SEM; $t_{(34)} = 0.1063$, $p = 0.9159$ (unpaired Student's *t* test). ***F***, Quantification of Smad fluorescence intensity/bouton area in the specified genotypes in ***C***, ***D***. Data are mean ± SEM; $t_{(34)} = 1.063$, $p = 0.2951$ (unpaired Student's *t* test). ***G–J***, Representative immunoblots showing total levels of Smad (***G***) and Trio (***H***), and corresponding quantification of ratio of band intensities of Smad (***I***) and Trio (***J***). ***I***, Data are mean ± SEM; $F_{(2,6)} = 31.42$, +/+ versus $dMegf8^{HSC}$: $p = 0.7653$, +/+ versus $wit^{-/-}$: $^{**}p = 0.0011$ (one-way ANOVA with Tukey's multiple comparisons). ***J***, Data are mean ± SEM; $t_{(4)} = 0.5412$, $p = 0.6171$ (unpaired Student's *t* test). ***K–R***, Confocal images in (***K***) *dMegf8* heterozygote ($dMegf8^{HSC+/-}$), (***L***) *dMegf8, dnrx* trans-heterozygote ($dMegf8^{HSC+/-};dnrx^{+/-}$), (***M***) $dnrx^{-/-}$ mutant, (***N***) *dMegf8, dnrx* double mutant ($dMegf8^{HSC-/-};dnrx^{-/-}$), (***O***) *wit* heterozygote ($wit^{+/-}$), (***P***) *dMegf8, wit* trans-heterozygote ($dMegf8^{HSC+/-};wit^{+/-}$), (***Q***) $wit^{-/-}$ mutant, and (***R***) *dMegf8, wit* double mutant ($dMegf8^{HSC-/-};wit^{-/-}$) third instar larval NMJ labeled with anti-Hrp (green) and anti-Dlg (red). ***S***, ***T***, Quantification of total bouton numbers in indicated genotypes. ***S***, Data are mean ± SEM; $F_{(6,107)} = 21.47$, +/+ versus $dMegf8^{+/-}$: $p > 0.9999$, +/+ versus $dnrx^{+/-}$: $p = 0.7589$, +/+ versus $dMegf8^{+/-};dnrx^{+/-}$: $^{****}p < 0.0001$, +/+ versus $dnrx^{-/-}$: $^{****}p < 0.0001$, +/+ versus $dMegf8^{-/-}$: $^{****}p < 0.0001$, +/+ versus $dMegf8^{-/-};dnrx^{-/-}$: $^{****}p < 0.0001$, $dMegf8^{+/-};dnrx^{+/-}$ versus $dnrx^{-/-}$: $p = 0.5614$, $dnrx^{-/-}$ versus $dMegf8^{-/-}$: $p = 0.9379$, $dnrx^{-/-}$ versus $dMegf8^{-/-};dnrx^{-/-}$: $p = 0.8967$ (one-way ANOVA test with Tukey's multiple comparisons). ***T***, Data are mean ± SEM; $F_{(7,120)} = 21.32$, +/+ versus $dMegf8^{+/-}$: $p = 0.9211$, +/+ versus $wit^{A12}/-$: $p = 0.9985$, +/+ versus $dMegf8^{+/-};wit^{A12}/-$: $^{***}p = 0.0009$, +/+ versus $dMegf8^{+/-};wit^{B11}/-$: $^{***}p = 0.0007$, +/+ versus $dMegf8^{-/-}$: $^{****}p < 0.0001$, +/+ versus $wit^{A12}/^{B11}$: $^{****}p < 0.0001$, +/+ versus $dMegf8^{-/-};wit^{A12}/^{B11}$: $^{****}p < 0.0001$, $dMegf8^{-/-}$ versus $wit^{A12/B11}$: $p = 0.9612$, $dMegf8^{-/-}$ versus $dMegf8^{-/-};wit^{A12/B11}$: $p = 0.9994$ (one-way ANOVA test with Tukey's multiple comparisons). Scale bars: ***A–H***, 20 μm.

whether dMegf8, Dnrx, and Wit existed as an *in vivo* biochemical complex and potentially function together. Therefore, we performed immunoblots and coimmunoprecipitations to resolve the question whether they formed a molecular complex. Immunoblots were performed both from adult fly heads (Fig. 8*A*,*B*,*D*) and third instar larval musculature that contains NMJs (Fig. 8*F*,*H*), mostly because the expression levels of dMegf8 and Dnrx in the larval musculature were too low to be detected. All coimmunoprecipitation analyses were performed using fly head lysates because of large amount of protein needed for these experiments.

First, we examined the total levels of dMegf8 in the *dMegf8* point mutation allele isolated from the ethyl methane sulfonate screen, $dMefg8^{F1}$ (Fig. 8*A*, quantified in Fig. 8*C*). dMegf8 levels were reduced by ~25% in $dMefg8^{F1}$ mutants compared with WT control (Fig. 8*A*, quantified in Fig. 8*C*). Immunoblotting analyses showed that dMegf8 levels (Fig. 8*B*, quantified in Fig. 8*C*) were not significantly affected in *dnrx* mutants (Fig. 8*B*, quantified in Fig. 8*C*). Likewise, Dnrx levels (Fig. 8*D*, quantified in Fig. 8*E*) levels were not significantly altered in *dMegf8* mutants compared with the WT in the fly head lysate preparations, indicating that in the adult head lysates the protein levels of dMegf8 and Dnrx were not affected in each other's mutants. We next tested the levels of Wit in WT and loss- and gain-of *dMegf8* backgrounds using the larval musculature (Fig. 8*F*,*H*). The total levels of Wit were significantly decreased in $dMegf8^{HSC}$ mutants compared with WT (Fig. 8*F*, quantified in Fig. 8*G*). Wit levels were significantly elevated in presynaptic *dMegf8* overexpression (Fig. 8*F*, quantified in Fig. 8*G*). Also, consistent with the finding that Wit fluorescence levels were reduced at NMJ (Fig. 6), total levels of Wit from lysates of Wit overexpression in *dMegf8* mutant background (*elav-Gal4;UAS-wit;*$dMegf8^{-/-}$)

were also significantly decreased when compared with Wit overexpression in the WT background (Fig. 8*H*, quantified in Fig. 8*I*), indicating that dMegf8 loss led to a significant reduction in total Wit levels. Actin was used as loading control for all immunoblots (Fig. 8*A*,*B*,*D*,*F*,*H*).

For coimmunoprecipitation analyses, because of the extremely low level of dMegf8 expression, no association with dMegf8 and Dnrx/Wit was observed with coimmunoprecipitations using antibodies to endogenous proteins at normal levels. To overcome this, we used adult head lysates from presynaptic *dMegf8* overexpression to test whether Dnrx and Wit would coprecipitate dMegf8. As shown in Figure 8*J*, immunoblots of *dMegf8* show IP with Dnrx antibodies coprecipitated dMegf8 from dMegf8 overexpression lysates, which was absent from *dnrx* mutant IPs confirming the association between dMegf8 and Dnrx. Coimmunoprecipitation with anti-Wit monoclonal antibodies also detected dMegf8 from dMegf8 overexpression lysates, which was absent in the Protein-A bead controls (Fig. 8*K*). IP using Dnrx and Wit antibodies efficiently precipitated Dnrx and Wit, respectively (data not shown) (Banerjee et al., 2017). Together, these results demonstrate that dMegf8, Dnrx, and Wit exist *in vivo* as a molecular complex and may function together in synaptic organization and function.

Discussion

Many neurodevelopmental and psychiatric disorders have been associated with disturbances in synaptic organization and function (Nanou and Catterall, 2018; Batool et al., 2019; Parenti et al., 2020). Since CS subjects show intellectual disabilities (Taravath and Tonsgard, 1993; Twigg et al., 2012; Giacopuzzi et al., 2017), it has remained unknown whether human MEGF8 will have a role in synaptic function. Our characterization of *dMegf8* in the neuromuscular synapses provides the first evidence that Megf8 proteins have synaptic functions. Our findings reveal that *dMegf8* mutants have multiple abnormalities in synaptic development, ultrastructural organization, and physiological functions, and that dMegf8 forms a biochemical complex with two well-characterized synaptic proteins Dnrx and Wit. Our studies provide insights into possible human MEGF8 functions and lay the groundwork for further characterization of the mechanisms underlying the intellectual disabilities associated with the CS.

Megf8 in synaptic development and function

Megf8 has been linked to various developmental abnormalities, including congenital heart defects as well as neurodevelopmental and axon guidance defects with early lethality associated with the murine homozygous null allele (Engelhard et al., 2013; Kong et al., 2020; Wang et al., 2020). These phenotypes have pointed to defects in Hedgehog and BMP signaling pathways (Twigg et al., 2012; Engelhard et al., 2013; Lloyd et al., 2018; Kong et al., 2020; Wang et al., 2020). The $dMegf8^{HSC}$ mutants reported here produced viable and fertile adults with motor coordination deficits (Fig. 1), unlike the *dMegf8* null reported by Lloyd et al. (2018), showing a late larval lethality. Although both alleles were generated using CRISPR/Cas9 methodology, it remains to be seen whether genetic background or a second site mutation caused $dMegf8^{\Delta 8}$ lethality (Lloyd et al., 2018). Our studies provide evidence that dMegf8 plays an important role during *Drosophila* larval NMJ development as dMegf8 localizes in synaptic terminals both presynaptic and postsynaptically, and loss of *dMegf8* leads to synaptic undergrowth, while overexpression of *dMegf8* in neurons causes synaptic overgrowth

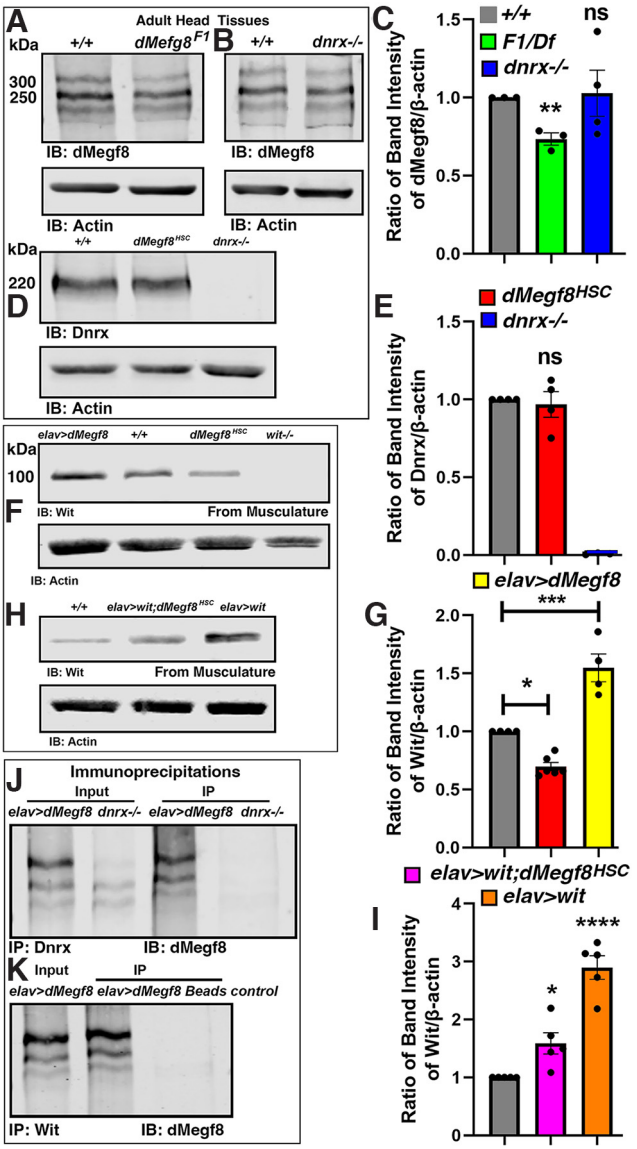

Figure 8. Biochemical interactions between dMegf8, Dnrx, and Wit. ***A–C***, Representative immunoblots from adult head lysates showing total levels of dMegf8 in WT (+/+), $dMegf8^{F1/Df}$ (***A***) and in *dnrx* mutant (***B***), and quantification of the normalized ratio of protein band intensities (***C***). +/+ versus $dMegf8^{F1}/Df$: $t_{(4)} = 6.815$, $^{**}p = 0.0024$ (unpaired Student's *t* test); +/+ versus $dnrx^{-/-}$: $t_{(6)} = 0.1961$, $p = 0.8510$ (unpaired Student's *t* test). ***D***, ***E***, Representative immunoblots from adult head lysates showing total levels of Dnrx in WT (+/+), $dMegf8^{HSC}$, and *dnrx* mutants (as a negative control), and quantification of the normalized ratio of protein band intensities (***E***). +/+ versus $dMegf8^{HSC}$: $t_{(6)} = 0.3921$, $p = 0.7085$ (unpaired Student's *t* test). ***F***, ***G***, Representative immunoblots from larval musculature lysates showing levels of Wit in specified genotypes, and quantification of the normalized ratio of protein band intensities (***G***). $F_{(2,11)} = 45.91$, +/+ versus $dMegf8^{HSC}$: $^{*}p = 0.0107$, +/+ versus *elav>dMegf8*: $^{***}p = 0.0003$ (one-way ANOVA test with Tukey's multiple comparisons). ***H***, ***I***, Representative immunoblots from larval musculature lysates showing levels of Wit in specified genotypes, and quantification of the normalized ratio of protein band intensities (***I***). $F_{(2,12)} = 37.98$, +/+ versus $elav>wit;dMegf8^{HSC}$: $^{*}p = 0.0396$, +/+ versus *elav>wit*: $^{****}p < 0.0001$ (one-way ANOVA test with Tukey's multiple comparisons). Actin was used as the loading control in ***A***, ***B***, ***D***, ***F***, ***H***. ***J***, ***K***, dMegf8 coimmunoprecipitated with anti-Dnrx (***J***) and anti-Wit (***K***) antibodies, respectively, and probed with anti-dMegf8. ***C***, ***E***, ***G***, ***I***, Data are mean ± SEM; $^{*}p < 0.05$; $^{**}p < 0.01$; $^{***}p < 0.001$; $^{****}p < 0.0001$; unpaired Student's *t* test (***C***, ***E***) and one-way ANOVA test with Tukey's multiple comparisons (***G***,***I***).

pointing to a presynaptic dMegf8 requirement. The synaptic undergrowth in *dMegf8* mutants is fully rescued by presynaptic and not by the postsynaptic expression of *dMegf8*, further demonstrating that *dMegf8* functions primarily in the presynaptic compartment.

While we did not see any disruption in the apposition of the presynaptic active zone protein, BRP, with the postsynaptic GluRIIA, the number of BRP-positive puncta/bouton area was significantly increased in *dMegf8* mutants, which was consistent with the ultrastructural analyses revealing increased active zones in *dMegf8* mutant synapses (see below). These findings are suggestive of a loss of dMegf8 impacting the proper organization of synaptic active zones. *dMegf8* mutants displayed diffuse Dlg distribution throughout the boutons unlike the peripheral rim of the boutons where Dlg normally localizes. Presynaptic expression of dMegf8 in $dMegf8^{HSC}$ mutants was able to restore Dlg localization better than the postsynaptic expression of dMegf8. Dlg has been previously shown to function both presynaptic and postsynaptically and loss of Dlg affects the SSR at the boutons (Budnik et al., 1996). The synaptic structural abnormalities are often accompanied by corresponding functional abnormalities. We observed significant reduction in the EJP amplitude and the quantal content in *dMegf8* mutants, which was restored by dMegf8 presynaptic and not by the postsynaptic expression. dMegf8 loss also affected the ultrastructural organization of the synapses with specific defects in the presynaptic elements as well as the postsynaptic specializations. Interestingly, restoration of dMegf8 expression either presynaptically or postsynaptically revealed that most functions of dMegf8 are presynaptic, except the SSR specialization, which was rescued by dMegf8 postsynaptic expression, suggesting that dMegf8 also has postsynaptic functions. Our studies are consistent with many of the synaptic phenotypes previously observed in mutations associated with genes involved in trans-synaptic functions (e.g., *dnrx, dnlg1, dnlg2*, and *wit*) (Aberle et al., 2002; McCabe et al., 2003; Li et al., 2007; Banovic et al., 2010; Chen et al., 2012; Banerjee et al., 2017), indicating that dMegf8 may be involved or functions in close association with these proteins. Our data thus provide insights that vertebrate Megf8 may also play an essential role in synaptic function as human MEGF8 has been linked to neurodevelopmental and psychiatric disorders. As our studies highlight the synaptic role of dMegf8 at the NMJs, it is possible that dMegf8 also functions in proper axonal growth, guidance, maturation, and fasciculation during neuronal development. As reported previously, CS patients present multiple developmental anomalies in addition to the intellectual disabilities (Engelhard et al., 2013), it is plausible that human MEGF8 might be involved in a plethora of functions in the developing nervous system ranging from neuronal survival, axon growth, guidance, maturation, fasciculation, target innervation, and synapse formation. Future studies on dMegf8 will explore its functions in some of these neural development processes.

dMegf8 and BMP signaling at the NMJ

The dMegf8 primary structure and its synaptic localization and the NMJ synaptic defects observed in *dMegf8* mutants suggested that it could potentially interact with other known synaptic proteins. Our immunohistochemical analyses showed that the absence of dMegf8 or Dnrx leads to their diffuse synaptic localization as well as protein instability in each other's mutant backgrounds (refer Fig. 6). However, the immunoblot analysis of dMegf8 or Dnrx did not show any variation in overall levels in each other's mutant backgrounds (Fig. 8), suggesting that,

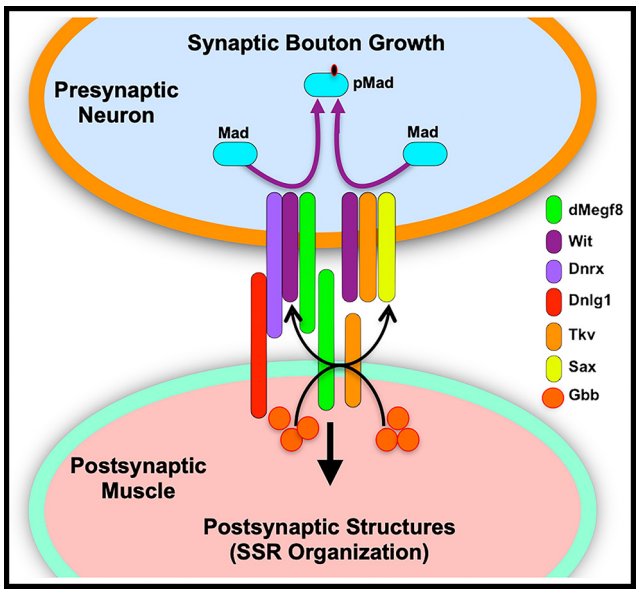

Figure 9. Schematic model of dMegf8 function at the NMJ synapse. A schematic model depicting dMegf8 and other known presynaptic and postsynaptic proteins at the NMJ. Based on our immunohistochemical, ultrastructural, electrophysiological, biochemical, and genetic rescue analyses, we propose that dMegf8 functions presynaptically to coordinate BMP signaling for the synaptic bouton growth and postsynaptically to organize the SSR and other synaptic structures that are necessary for proper synaptic function. While dMegf8 interactions with Dnrx and Wit are established, uncovering potential molecular interactions between dMegf8 and Dnlg1, Tkv, and Sax, or other synaptic proteins would shed further light on the functions of dMegf8 at the synapse.

despite the total protein levels remaining unchanged, dMegf8 and Dnrx fail to properly localize and cluster at the NMJ terminals and remain diffuse indicating that dMegf8 and Dnrx are mutually required for their proper synaptic localization. This is also reflected by the reduced levels of Wit in *dMegf8* mutants, indicating that loss of dMegf8 affects Wit localization and/or its stability at the NMJ. Together, these data underscore the important role that dMegf8 plays in the proper localization of other synaptic proteins and suggest interdependency of dMegf8, Dnrx, and Wit for their proper subcellular localization and/or stability at the NMJ.

Previously, Dnrx was shown to be essential for proper synaptic growth (Li et al., 2007; Südhof, 2008), and regulation of the BMP signaling pathway in coordination with BMP Type II receptor, Wit (Banerjee et al., 2017; Banerjee and Riordan, 2018). Interestingly, the murine Megf8 has also been shown to function as a modifier of BMP4 signaling in the trigeminal ganglion neurons (Engelhard et al., 2013). These observations suggest that dMegf8 along with other proteins is involved in BMP signaling. This is further strengthened by our genetic analysis, which revealed that *dMegf8* displays genetic interactions *dnrx* and *wit*, and that trans-heterozygous combinations of $dMegf8^{HSC+/-}$; $dnrx^{+/-}$ and $dMegf8^{HSC+/-}$;$wit^{+/-}$ displayed a significant reduction in bouton growth compared with the single heterozygotes, supporting the possibility that these genes function together in a dose-dependent manner. Furthermore, double mutants of $dMegf8^{HSC-/-}$;$dnrx^{-/-}$ and $dMegf8^{HSC-/-}$,$wit^{-/-}$ showed no significant differences in the bouton counts compared with their single mutants. These findings strongly support that *dMegf8*, *dnrx*, and *wit* function cooperatively to coordinate synaptic growth. Interestingly, however, there was no significant difference in pMad localization either in the VNC or at the NMJ or Trio levels in *dMegf8* mutants

compared with WT (Fig. 7). One of the possibilities might be that dMegf8 works with Dnrx and Wit in a large complex structurally to regulate synaptic development, but not participate directly in signaling functions as part of the BMP pathway (Fig. 9). Another possibility is that, although the proper localization and stability of Wit requires dMegf8, other BMP receptors, such as Tkv and Sax, could still function effectively to activate downstream signaling of the BMP pathway. Thus, dMegf8 may function presynaptically to coordinate BMP signaling to ensure normal synaptic bouton growth and also postsynaptically to organize the SSR and other postsynaptic structures, which are both necessary for proper synaptic function. A more detailed analyses of some of these questions will be addressed as part of our future investigations.

dMegf8 molecular complex

Previous studies on Megf8 have not reported any biochemical interactions with other proteins that would link Megf8 to neuronal functions. Our biochemical analyses of dMegf8 showed that dMegf8, Dnrx, and Wit exist in a large biochemical complex. While the overall levels of dMegf8 and Dnrx did not seem to change in each other's mutant backgrounds using adult head lysates, the levels of these proteins at the NMJ containing musculature are too low to detect any changes in their levels. Interestingly, the total levels of Wit using the musculature lysates were affected by the presence or absence of dMegf8, as presynaptic expression of dMegf8 increased Wit levels at the NMJ. As the endogenous dMegf8 levels were extremely low for the IP analysis, we used dMegf8 overexpression for IP, which revealed that dMegf8, Dnrx, and Wit form a large protein complex. How these proteins may interact with each other and what the stoichiometry of these interactions is remain to be fully investigated. Given the complex domain structure and large size of dMegf8, it is likely that dMegf8 interacts with a host of other presynaptic and postsynaptic proteins. It will be of significant interest to know what these proteins are and how they function in a macromolecular complex at the NMJ or other synapses. Further elucidation of the dMegf8 genetic and molecular functions and the signaling complexes that dMegf8 engages in will uncover the relevant functions of the human MEGF8 that is associated with deficits seen in the Carpenter syndrome or other psychiatric disorders.

References

Aberle H, Haghighi AP, Fetter RD, McCabe BD, Magalhaes TR, Goodman CS (2002) wishful thinking encodes a BMP Type II receptor that regulates synaptic growth in *Drosophila*. Neuron 33:545–558.

Alessandri JL, Dagoneau N, Laville JM, Baruteau J, Hebert JC, Cormier-Daire V (2010) RAB23 mutation in a large family from Comoros Islands with Carpenter syndrome. Am J Med Genet A 152A:982–986.

Awasaki T, Saito M, Sone M, Suzuki E, Sakai R, Ito K, Hama C (2000) The *Drosophila* trio plays an essential role in patterning of axons by regulating their directional extension. Neuron 26:119–131.

Ball RW, Warren-Paquin M, Tsurudome K, Liao EH, Elazzouzi F, Cavanagh C, An BS, Wang TT, White JH, Haghighi AP (2010) Retrograde BMP signaling controls synaptic growth at the NMJ by regulating trio expression in motor neurons. Neuron 66:536–549.

Banerjee S, Riordan M (2018) Coordinated regulation of axonal microtubule organization and transport by *Drosophila* neurexin and BMP pathway. Sci Rep 8:17337.

Banerjee S, Venkatesan A, Bhat MA (2017) Neurexin, Neuroligin and Wishful Thinking coordinate synaptic cytoarchitecture and growth at neuromuscular junctions. Mol Cell Neurosci 78:9–24.

Banovic D, Khorramshahi O, Owald D, Wichmann C, Riedt T, Fouquet W, Tian R, Sigrist SJ, Aberle H (2010) *Drosophila* neuroligin 1 promotes growth and postsynaptic differentiation at glutamatergic neuromuscular junctions. Neuron 66:724–738.

Batool S, Raza H, Zaidi J, Riaz S, Hasan S, Syed NI (2019) Synapse formation: from cellular and molecular mechanisms to neurodevelopmental and neurodegenerative disorders. J Neurophysiol 121:1381–1397.

Bayat V, Jaiswal M, Bellen HJ (2011) The BMP signaling pathway at the *Drosophila* neuromuscular junction and its links to neurodegenerative diseases. Curr Opin Neurobiol 21:182–188.

Bersani G, Maddalena F, Pasquini M, Orlandi V, Pancheri P (2003) Association of schizophrenia and Carpenter syndrome. Acta Neuropsychiatr 15:304–305.

Budnik V, Koh YH, Guan B, Hartmann B, Hough C, Woods D, Gorczyca M (1996) Regulation of synapse structure and function by the *Drosophila* tumor suppressor gene dlg. Neuron 17:627–640.

Carpenter G (1901) Two sisters showing malformations of the skull and other congenital abnormalities. Rep Soc Study Dis Child Lond 1:9.

Chen YC, Lin YQ, Banerjee S, Venken K, Li J, Ismat A, Chen K, Duraine L, Bellen HJ, Bhat MA (2012) *Drosophila* neuroligin 2 is required presynaptically and postsynaptically for proper synaptic differentiation and synaptic transmission. J Neurosci 32:16018–16030.

Chittaranjan S, McConechy M, Hou YC, Freeman JD, Devorkin L, Gorski SM (2009) Steroid hormone control of cell death and cell survival: molecular insights using RNAi. PLoS Genet 5:e1000379.

Cox DM, Butler MG (2015) A clinical case report and literature review of the 3q29 microdeletion syndrome. Clin Dysmorphol 24:89–94.

Dudu V, Bittig T, Entchev E, Kicheva A, Julicher F, Gonzalez-Gaitan M (2006) Postsynaptic mad signaling at the *Drosophila* neuromuscular junction. Curr Biol 16:625–635.

Engelhard C, Sarsfield S, Merte J, Wang Q, Li P, Beppu H, Kolodkin AL, Sucov HM, Ginty DD (2013) MEGF8 is a modifier of BMP signaling in trigeminal sensory neurons. Elife 2:e01160.

Feeney CJ, Karunanithi S, Pearce J, Govind CK, Atwood HL (1998) Motor nerve terminals on abdominal muscles in larval flesh flies, *Sarcophaga bullata*: comparisons with *Drosophila*. J Comp Neurol 402:197–209.

Gargano JW, Martin I, Bhandari P, Grotewiel MS (2005) Rapid iterative negative geotaxis (RING): a new method for assessing age-related locomotor decline in *Drosophila*. Exp Gerontol 40:386–395.

Giacopuzzi E, Gennarelli M, Minelli A, Gardella R, Valsecchi P, Traversa M, Bonvicini C, Vita A, Sacchetti E, Magri C (2017) Exome sequencing in schizophrenic patients with high levels of homozygosity identifies novel and extremely rare mutations in the GABA/glutamatergic pathways. PLoS One 12:e0182778.

Guangming G, Junhua G, Chenchen Z, Yang M, Wei X (2020) Neurexin and neuroligins maintain the balance of ghost and satellite boutons at the *Drosophila* neuromuscular junction. Front Neuroanat 14:19.

Haye D, Collet C, Sembely-Taveau C, Haddad G, Denis C, Soule N, Suc AL, Listrat A, Toutain A (2014) Prenatal findings in Carpenter syndrome and a novel mutation in RAB23. Am J Med Genet A 164A:2926–2930.

Hidestrand P, Vasconez H, Cottrill C (2009) Carpenter syndrome. J Craniofac Surg 20:254–256.

Jenkins D, et al. (2007) RAB23 mutations in Carpenter syndrome imply an unexpected role for hedgehog signaling in cranial-suture development and obesity. Am J Hum Genet 80:1162–1170.

Jia XX, Gorczyca M, Budnik V (1993) Ultrastructure of neuromuscular junctions in *Drosophila*: comparison of wild type and mutants with increased excitability. J Neurobiol 24:1025–1044.

Kong JH, et al. (2020) A membrane-tethered ubiquitination pathway regulates hedgehog signaling and heart development. Dev Cell 55:432–449. e412.

Lahey T, Gorczyca M, Jia XX, Budnik V (1994) The *Drosophila* tumor suppressor gene dlg is required for normal synaptic bouton structure. Neuron 13:823–835.

Li J, Ashley J, Budnik V, Bhat MA (2007) Crucial role of *Drosophila* neurexin in proper active zone apposition to postsynaptic densities, synaptic growth, and synaptic transmission. Neuron 55:741–755.

Lloyd DL, Toegel M, Fulga TA, Wilkie AO (2018) The *Drosophila* homologue of MEGF8 is essential for early development. Sci Rep 8:8790.

Marques G, Bao H, Haerry TE, Shimell MJ, Duchek P, Zhang B, O'Connor MB (2002) The *Drosophila* BMP Type II receptor Wishful Thinking regulates neuromuscular synapse morphology and function. Neuron 33:529–543.

Marrus SB, Portman SL, Allen MJ, Moffat KG, DiAntonio A (2004) Differential localization of glutamate receptor subunits at the *Drosophila* neuromuscular junction. J Neurosci 24:1406–1415.

McCabe BD, Marques G, Haghighi AP, Fetter RD, Crotty ML, Haerry TE, Goodman CS, O'Connor MB (2003) The BMP homolog Gbb provides a retrograde signal that regulates synaptic growth at the *Drosophila* neuromuscular junction. Neuron 39:241–254.

Mummery-Widmer JL, Yamazaki M, Stoeger T, Novatchkova M, Bhalerao S, Chen D, Dietzl G, Dickson BJ, Knoblich JA (2009) Genome-wide analysis of Notch signalling in *Drosophila* by transgenic RNAi. Nature 458:987–992.

Nahm M, et al. (2013) Spartin regulates synaptic growth and neuronal survival by inhibiting BMP-mediated microtubule stabilization. Neuron 77:680–695.

Nanou E, Catterall WA (2018) Calcium channels, synaptic plasticity, and neuropsychiatric disease. Neuron 98:466–481.

Obi-Nagata K, Temma Y, Hayashi-Takagi A (2019) Synaptic functions and their disruption in schizophrenia: from clinical evidence to synaptic optogenetics in an animal model. Proc Jpn Acad Ser B Phys Biol Sci 95:179–197.

Pan C, et al. (2014) Targeted discovery and validation of plasma biomarkers of Parkinson's disease. J Proteome Res 13:4535–4545.

Parenti I, Rabaneda LG, Schoen H, Novarino G (2020) Neurodevelopmental disorders: from genetics to functional pathways. Trends Neurosci 43:608–621.

Pazos Obregon F, Papalardo C, Castro S, Guerberoff G, Cantera R (2015) Putative synaptic genes defined from a *Drosophila* whole body developmental transcriptome by a machine learning approach. BMC Genomics 16:694.

Pusapati GV, Kong JH, Patel BB, Krishnan A, Sagner A, Kinnebrew M, Briscoe J, Aravind L, Rohatgi R (2018) CRISPR screens uncover genes that regulate target cell sensitivity to the morphogen sonic hedgehog. Dev Cell 44:113–129.e118.

Ruiz-Canada C, Budnik V (2006) Introduction on the use of the *Drosophila* embryonic/larval neuromuscular junction as a model system to study synapse development and function, and a brief summary of pathfinding and target recognition. Int Rev Neurobiol 75:1–31.

Shi Q, Lin YQ, Saliba A, Xie J, Neely GG, Banerjee S (2019) Tubulin polymerization promoting protein, Ringmaker, and MAP1B homolog Futsch coordinate microtubule organization and synaptic growth. Front Cell Neurosci 13:192.

Stewart BA, Atwood HL, Renger JJ, Wang J, Wu CF (1994) Improved stability of *Drosophila* larval neuromuscular preparations in haemolymph-like physiological solutions. J Comp Physiol A Neuroethol Sens Neural Behav Physiol 175:179–191.

Südhof TC (2008) Neuroligins and neurexins link synaptic function to cognitive disease. Nature 455:903–911.

Sun M, Xie W (2012) Cell adhesion molecules in *Drosophila* synapse development and function. Sci China Life Sci 55:20–26.

Taravath S, Tonsgard JH (1993) Cerebral malformations in Carpenter syndrome. Pediatr Neurol 9:230–234.

Twigg SR, et al. (2012) Mutations in multidomain protein MEGF8 identify a Carpenter syndrome subtype associated with defective lateralization. Am J Hum Genet 91:897–905.

Valnegri P, Sala C, Passafaro M (2012) Synaptic dysfunction and intellectual disability. Adv Exp Med Biol 970:433–449.

Wagh DA, et al. (2006) Bruchpilot, a protein with homology to ELKS/CAST, is required for structural integrity and function of synaptic active zones in *Drosophila*. Neuron 49:833–844.

Wang W, Zheng X, Song H, Yang J, Liu X, Wang Y, Zhang M, Zhang Z (2020) Spatial and temporal deletion reveals a latent effect of Megf8 on the left-right patterning and heart development. Differentiation 113:19–25.

Weyhersmuller A, Hallermann S, Wagner N, Eilers J (2011) Rapid active zone remodeling during synaptic plasticity. J Neurosci 31:6041–6052.

Wu H, Xiong WC, Mei L (2010) To build a synapse: signaling pathways in neuromuscular junction assembly. Development 137:1017–1033.

Xie J, Chen S, Bopassa JC, Banerjee S (2021) *Drosophila* tubulin polymerization promoting protein mutants reveal pathological correlates relevant to human Parkinson's disease. Sci Rep 11:13614.

Xue M, Lin YQ, Pan H, Reim K, Deng H, Bellen HJ, Rosenmund C (2009) Tilting the balance between facilitatory and inhibitory functions of mammalian and *Drosophila* Complexins orchestrates synaptic vesicle exocytosis. Neuron 64:367–380.

Zeng X, Sun M, Liu L, Chen F, Wei L, Xie W (2007) Neurexin-1 is required for synapse formation and larvae associative learning in *Drosophila*. FEBS Lett 581:2509–2516.

Zhang X, Koolhaas WH, Schnorrer F (2014) A versatile two-step CRISPR- and RMCE-based strategy for efficient genome engineering in *Drosophila*. G3 (Bethesda) 4:2409–2418.